

# Sheffield Hallam University

*Investigation into the effects of chromium cross-contamination in niobium sputter deposited coatings using a multi-target PVD system.*

JARRATT, Mark.

Available from the Sheffield Hallam University Research Archive (SHURA) at:

<http://shura.shu.ac.uk/19869/>

## A Sheffield Hallam University thesis

This thesis is protected by copyright which belongs to the author.

The content must not be changed in any way or sold commercially in any format or medium without the formal permission of the author.

When referring to this work, full bibliographic details including the author, title, awarding institution and date of the thesis must be given.

Please visit <http://shura.shu.ac.uk/19869/> and <http://shura.shu.ac.uk/information.html> for further details about copyright and re-use permissions.

CITY CAMPUS, POND STREET,  
ENFIELD, ST. MRS.

101 617 300 8



**REFERENCE**

ProQuest Number: 10697175

All rights reserved

INFORMATION TO ALL USERS

The quality of this reproduction is dependent upon the quality of the copy submitted.

In the unlikely event that the author did not send a complete manuscript and there are missing pages, these will be noted. Also, if material had to be removed, a note will indicate the deletion.



ProQuest 10697175

Published by ProQuest LLC (2017). Copyright of the Dissertation is held by the Author.

All rights reserved.

This work is protected against unauthorized copying under Title 17, United States Code  
Microform Edition © ProQuest LLC.

ProQuest LLC.  
789 East Eisenhower Parkway  
P.O. Box 1346  
Ann Arbor, MI 48106 – 1346

**INVESTIGATION INTO THE  
EFFECTS OF CHROMIUM CROSS-  
CONTAMINATION IN NIOBIUM  
SPUTTER DEPOSITED COATINGS  
USING A MULTI-TARGET PVD  
SYSTEM**

**Mark Jarratt**

**A thesis submitted in partial fulfilment of the  
requirements of Sheffield Hallam University for  
the degree of Master of Philosophy**

**May 1998**



LEVEL 1

# CONTENTS

Title Page.....	(i)
Abstract.....	(ii)
Acknowledgements.....	(iii)
<b>1. INTRODUCTION.....</b>	<b>1</b>
1.1 Introduction.....	1
1.2 Physical Vapour Deposition.....	1
<b>2. LITERATURE REVIEW.....</b>	<b>3</b>
2.1 Introduction.....	3
2.2 The Coating Process.....	3
2.2.1 The Hauzer HTC 1000-4 ABS™.....	3
2.2.2 Sputtering Techniques.....	6
2.2.3 D.C. Glow Discharge.....	9
2.2.4 D.C. Diode sputtering.....	13
2.2.5 Magnetron sputtering deposition.....	15
2.2.6 Unbalanced Magnetron.....	18
2.2.7 Closed Field Systems.....	19
2.3 Coating Deposition, Structure and Properties.....	21
2.3.1 Film Growth.....	21
2.3.2 The microstructures of the sputter deposited films.....	22
2.3.3 Ar <sup>+</sup> Sputter Etching.....	24
2.3.4 Crystallographic Texture.....	24
2.3.5 Residual Stress.....	25
2.3.6 Grain Growth Driving Mechanisms.....	26
2.3.7 Solid Solutions.....	27
2.3.8 Cross-Contamination.....	28

2.4	Coating Materials.....	29
	Niobium-Chromium system.....	29
2.5	Coating Performance.....	30
2.5.1	Corrosion Resistance.....	30
2.5.2	Friction and Wear.....	31
2.5.3	Microhardness.....	31
<b>3.</b>	<b>EXPERIMENTAL TECHNIQUE.....</b>	<b>32</b>
3.1	Experimental Design.....	32
3.2	Sample Preparation for Coating.....	33
3.3	Process Details.....	34
3.4	Techniques used to Characterise Coatings.....	36
3.4.1	X-Ray Diffraction, (XRD).....	36
	Crystallographic Texture.....	36
	Omega Scan.....	37
	Asymmetric Bragg-Brentano Stress Analysis.....	37
	Glancing Angle X-Ray diffraction, (GXRd).....	38
	Line Broadening Analysis.....	38
3.4.2	Glow Discharge Optical Emission Spectroscopy, (GDOES).....	39
3.4.3	Scanning Electron Microscope, SEM.....	40
3.4.4	Corrosion Test.....	40
3.4.5	Microhardness Test.....	41
3.4.6	Rockwell Indentation Adhesion Test.....	41
3.4.7	Friction Test.....	42
<b>4.</b>	<b>RESULTS.....</b>	<b>43</b>
4.1	GDOES results.....	43
4.2	X-Ray Diffraction Analysis.....	51

## Abstract

The optimisation of the tribological properties of engineering components has led to the development of a number of surface coating techniques. One such technique is Physical Vapour Deposition (PVD) which has proved to be a consistently reliable method for the production of thin coatings. The PVD coating system used in this study was the Hauzer HTC 1000-4 ABS™ which utilises four unbalanced magnetrons in closed-field geometry.

A typical coating process uses Arc evaporation to clean the substrates prior to deposition and can involve the use of a target for this stage that is not required during the coating process. During deposition to prevent unused targets becoming coated a negative potential is applied to the cathodes. As a result, due to the lack of individual target shutters, the possibility of cross-contamination between targets of different metals therefore arises.

This thesis describes research into the existence and possible effects of Cr cross-contamination on the physical properties of Nb coatings on M2 High Speed Steel (HSS) and 304 bright annealed stainless steel substrates.

During this investigation coatings were co-sputter deposited using a main Nb target power of 8kW and Cr target voltages of 0-350V in increments of 25/50V, (the potential range commonly used to prevent unwanted deposition on unused targets), at a temperature of ~400°C.

The subsequent coatings were characterised using Glow Discharge Optical Emission Spectroscopy, GDOES to determine depth profiles of chemical composition, and X-Ray Diffraction, XRD to determine the structure and to give an indication of the intrinsic stress and texture of the coatings. Other testing methods included Rockwell indentation, Universal hardness, and corrosion tests.

GDOES indicated levels of Cr at or below the limit of calibration at target voltages below 200V. Above this potential an increase in the atomic % of Cr was found at the coating/substrate interface which increased as the potential was increased. This was attributed to the initially clean Cr target's higher sputter yield. XRD indicated body centred cubic structure for all coatings, a pronounced minimum in the intrinsic stress in the coatings when using a Cr target voltage of 150V. A reduction in the (110) texture of the coatings was initially also observed for this target voltage, however, subsequent repeat coatings failed to show the same behaviour. This reproducibility failure may be due to changes in the set-up of the vacuum chamber between processes. Rockwell tests indicated good adhesion. Ultramicrohardness tests were inconclusive, probably due to the thickness of the coatings which were approximately 400nm for all samples. Corrosion tests showed improved resistance to alkaline attack for the samples with increasing atomic % Cr with the best corrosion results observed for the coating deposited using a Cr target voltage of 350V.

## ACKNOWLEDGEMENTS

I would like to thank the following people for their help, advice and encouragement during my period of study:

Director of Studies Prof. W.-D. Münz, Materials Research Institute, Sheffield Hallam University and my second supervisor Dr. J. Young, School of Science and Mathematics, Sheffield Hallam University.

Dr. B. Lewis, Materials Research Institute, Sheffield Hallam University

Mr. C. Rebholz, Surface Engineering department, Hull University

Mr. K. Blake, Dr. P. Walke, Dr. L. Donohue, Miss H. Paritong and the rest of the staff and research students at the Materials Research Institute

Mr. I. Owen, Mr. S. Hodgson and the rest of the staff in the School of Science and Mathematics

Finally, I would like to thank my mother, father and family for their constant support

# Chapter 1

## 1. Introduction

### 1.1. Surface Engineering

To improve the overall performance and efficiency of engineering components there have been great advancements in the field of surface engineering. A large number of industrial techniques are available to produce thin coatings deposited on suitable substrates. Traditional methods such as simple painting techniques and electro-plating have been used extensively for the last 100 years. However they have a limited range of coatings that they can deposit and the possibility of serious environmental pollution exists from chemical by-products. A specific surface engineering technique which has proved to be commercially successful and which does not suffer from these problems is physical vapour deposition (PVD).

### 1.2. Physical Vapour Deposition

The generic term physical vapour deposition (PVD) covers a range of techniques where, under vacuum, the coating species is atomised by thermal energy or particle bombardment. Metals, alloys, ceramics and non-conducting coatings can be deposited at relatively low temperatures (150-500°C) on a large range of temperature-sensitive substrates. The two main deposition techniques are sputtering (1) and evaporation (2). This thesis, is concerned only with sputtering.

Sputter PVD involves the atomisation of coating material from a solid target by energetic bombardment with ions or neutral particles. The surface atoms are ejected due to momentum transfer and condense on a suitable substrate.

A problem which has been encountered with multi-target PVD systems without individual target shutters is the unwanted deposition of target material onto unused targets. In the PVD system used in this study, the Hauzer HTC-1000 (3) unused targets are masked with

Aluminium foil, however if they are to be used at some point during coating a voltage is applied to the targets which are not in use to re sputter any deposited material.

However, this can result in the sputtering of unwanted target material, so called cross-contamination. This primary objective of this thesis was to investigate whether potentials of the magnitude used to prevent unwanted deposition on unused Chromium, Cr targets during Niobium, Nb deposition are sufficient to cause sputtering and therefore Chromium contamination. If Cr contamination was detected the secondary objective would be to determine the effect of the contaminant on the stress, texture, hardness and corrosion resistance of the resultant coatings.

## Chapter 2

### 2. Literature Review

#### 2.1 Introduction

The primary aim of this research was to study the effect on coating structure and properties of cross-contamination between targets of different metals in the Hauzer HTC 1000-4 ABS™ coater, in particular in the Nb-Cr bi-metallic system.

A review of the literature indicates there have been no reported studies of the effects of such contamination in this or other sputtering systems. Therefore this review addresses key processes and issues involved in this study, in particular, (a) the design and operation of the ABS™ system and, (b) the fundamentals of the coating process, including sputtering, glow discharge, closed-field unbalanced magnetron and coating deposition and (c) the resulting microstructure of the deposited coatings.

#### 2.2 The Coating Process

##### 2.2.1 The Hauzer HTC 1000-4 ABS™ (4)

The equipment used to deposit the coatings was the Hauzer HTC 1000-4 ABS™ (Arc Bond Sputtering) which combines unbalanced magnetron and cathodic arc technology within a single unit (figure 2.1). This enables the production of coatings with excellent adhesion properties, via the arc, with the versatility of coating materials given by a magnetron source. However, for the purposes of this research, the coatings were deposited via magnetron alone so as not to mask potential cross-contamination at the substrate/coating interface.

The octagonally shaped vacuum chamber of the Hauzer HTC 1000-4 ABS™ system has a diagonal distance between the targets of 1000 mm and a height of 1000 mm, giving a

chamber of total volume 800 l. The substrate to target distance is 300mm and the walls are 25 mm thick stainless steel. Figure 2.2 shows a schematic cross-section of the vacuum chamber.

The coater is equipped with two turbomolecular pumps with oil lubricant bearings and inert-gas sealing working in combination with a roots pump and a rotary-vane pump. To avoid the effect of 'shadowing', which produces non-uniform coatings, the substrate table is geared for three-fold planetary rotation.

### **Cathodes**

The ABS™ system uses four cathodes positioned perpendicular to one another and mounted in pairs in the two vacuum chamber doors, each with target dimensions of 600 mm x 190 mm. Each of these cathodes is connected to its own individual power supply, which can provide 80V / 100A in arc mode and 750V / 40A in magnetron mode. The power density accepted for each cathode is at least  $10\text{Wcm}^{-2}$  for an acceptable coating rate.

A schematic diagram of one of the cathodes is given in figure 2.1. It shows the vacuum chamber wall (1), electromagnetic coils (2), (which allow the degree of unbalance to be altered via the applied coil current), target (3), magnetic yoke (4) and the centre pole fixturing (5). By moving the outer magnets away from the target along the fixturing the cathode converts from magnetron to arc mode.

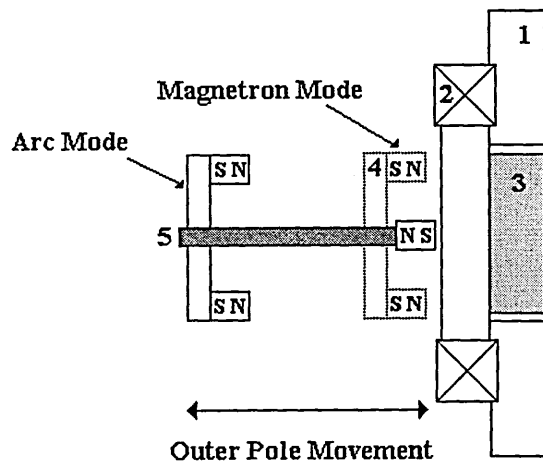


**Figure 2.1 Schematic diagram of an ABS™ cathode**

The ABS™ system is equipped with movable shutters which cover the targets. In Unbalanced Magnetron, UBM mode, they avoid a pre-coating of the substrate during the target cleaning step and in arc mode they avoid droplets reaching the substrate. The shutters are at floating potential, so as not to reduce the number of electrons and ions in the chamber. To optimise the efficiency of the shutters, they are positioned quite close to the targets. However, they are inter-linked so individual unused targets, which may have been used in the etch stage cannot be protected during the sputter deposition process. In practice, a certain voltage is applied to prevent the target becoming coated. In section 3.1 the effect of this target voltage on the resultant coating is investigated.

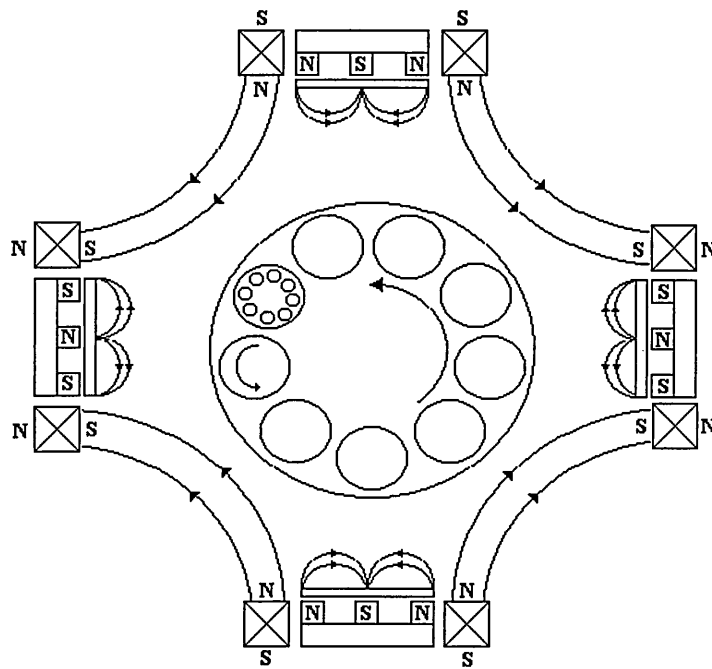


**Figure 2.2 Schematic of the ABS coater showing the closed-field geometry**

### 2.2.2 Sputtering Techniques

Sputtering is the removal of surface atoms from a solid when it is bombarded with energetic ions or neutral particles (4). W.R.Grove (5) first discovered the phenomenon of sputtering in 1842 after noticing metallic deposition on the walls of a discharge tube accompanied by cathodic erosion. However, it wasn't until 1902 that work on the physical process of sputtering was published (6) and another fifty years elapsed before a quantitative description of the phenomena could be developed (7).

In general, sputtering is a process whereby surface atoms are dislodged and ejected from a solid surface due to a momentum exchange associated with the bombardment of the surface by energetic particles. The momentum exchange occurs primarily within a region extending to about 1 nm below the surface. The energy transfer from the incident particle to the atomic nuclei is given for a binary collision by (13):

$$T = \frac{4m_i m_t}{(m_i + m_t)^2} E_0 \sin^2 \frac{\Theta}{2} \quad \dots \text{equation 2.1}$$

where T is the energy transfer function for a binary collision,  $m_i$  and  $m_t$  are the masses of the incident and target atoms,  $\Theta$ , is the projectile scattering angle and  $E_0$  the initial energy of the atom.

If the energy transferred from the incoming particle to the surface atoms is sufficient to overcome the lattice point binding energy, a collision cascade is formed due to the creation of primary recoil atoms. Sputtering of the surface atoms occurs if the energy transferred normal to the surface is sufficient to overcome the surface binding energy.

The sputtering efficiency of a target material is measured using a quantity known as the sputtering yield, (Y) which is defined as the mean number of atoms removed from the target per incident particle (8):

$$Y = \frac{\text{number of atoms removed}}{\text{number of incident particles}} \quad \dots \text{equation 2.2}$$

The yield is determined for a particular target material using ions as they are easy to accelerate in glow discharge. However, there may also be neutral atoms, electrons or energetic photons present.

The yield, which is a function of the energy of the incident ions (9), (the Hauzer ABS<sup>TM</sup> (4) uses  $\text{Ar}^+$ ), target material characteristics, incidence angle, ion energy and ion mass may be expressed as (10):

$$Y = \frac{3E_t \alpha E_i}{4\pi^2 U_0} \quad \dots \text{equation 2.3}$$

where  $E_i$  is the energy of the incident ion,  $\alpha$  is a function of the colliding atom masses,  $E_t$  is the energy transferred in a binary collision, and  $U_0$  the surface binding energy of the target.

When the energy of an ion is increased from a threshold energy, say of 20eV to 100eV, the sputtering yield rises rapidly. As the energy is increased further the sputtering yield increases almost linearly and the deposition of films on a substrate is possible (11). However the dependence of  $Y$  on the incident energy reduces if the ion energy is increased further, due to increased ion penetration (12).

Apart from the ejection of sputtered material energetic ion bombardment can cause a number of other physical interaction events to occur at the target surface, (13) as summarised by figure 2.3. These include the liberation of neutral atoms, backscattering, X-ray emission, photon generation, secondary electron emission, and desorption of gas atoms. Further, several effects can occur within the target itself including amorphisation, implantation, compound formation, localised heating and the creation of point defects.

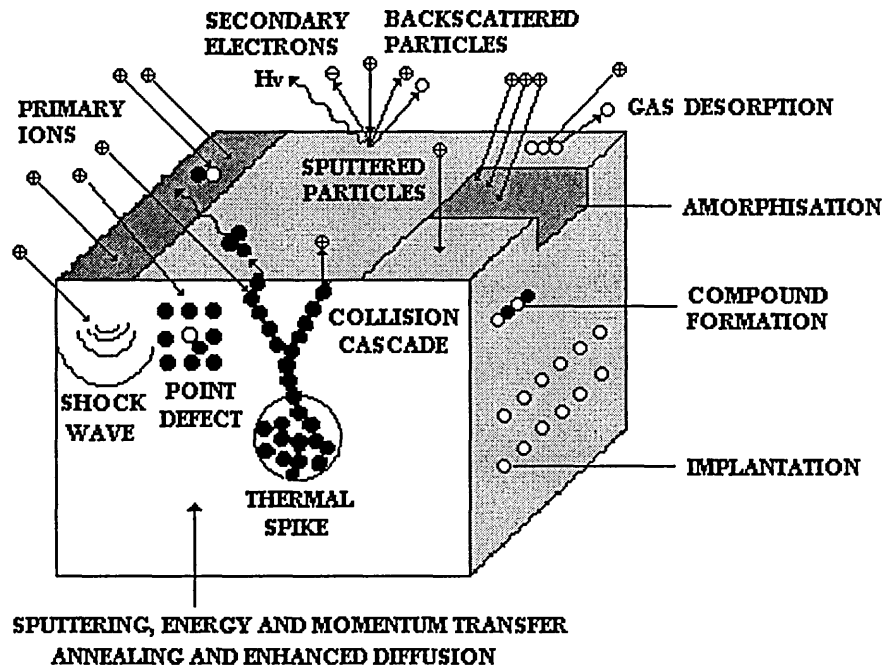


Figure 2.3 Interaction events at the target due to bombardment of energetic particles

The sputtering process has distinct advantages over other coating processes, such as evaporation, as there is virtually no restriction on which target materials which can be used (12). Higher thickness uniformity is achieved over larger target areas, and smoother films are possible due to the lack of macro-particle formation.

### **2.2.3 D.C. Diode Glow discharge**

The diode plasma known as a “glow discharge” is an electrically-neutral, partially- ionised gas commonly used in the PVD process. It can be formed under vacuum by applying a high voltage (~300-5000V) between two electrodes in the presence of a gas, usually argon (14). A small portion of the gas will be naturally ionised due to background cosmic radiation. These ions are accelerated towards the cathode (the target of the material to be deposited) and the electrons accelerated towards the anode, (the vacuum chamber wall). When the accelerated ions collide with the cathode most of their energy is lost in the form of heat, they may lose their charge and they can also be elastically recoiled or implanted. However, a small part of their incident energy can be transferred to the near surface cathode atoms which can result in the ejection of target atoms by the sputtering process.

The discharge can be sustained due to the liberation of secondary electrons from the target due to ion bombardment. These electrons are attracted towards the grounded chamber walls and as they move through the vacuum, they cause further ionisation events, together with the dissociation and excitation of the argon atoms, thus sustaining the discharge.

The typical secondary electron yield for Ar and a pure metal target in a sputtering process is 0.1 (14). The secondary electrons are easily accelerated by the applied electric field due to their low mass and are quickly lost to the chamber walls. Therefore the probability of further ionisation events needed to sustain the discharge is low. It can be seen that the diode sputtering process is therefore highly inefficient. However, modifications to the diode arrangement have significantly increased its effectiveness these will be discussed in sections 2.5-2.7.

The typical current-voltage (I-V) relationship for a glow discharge is shown by, fig 2.4.

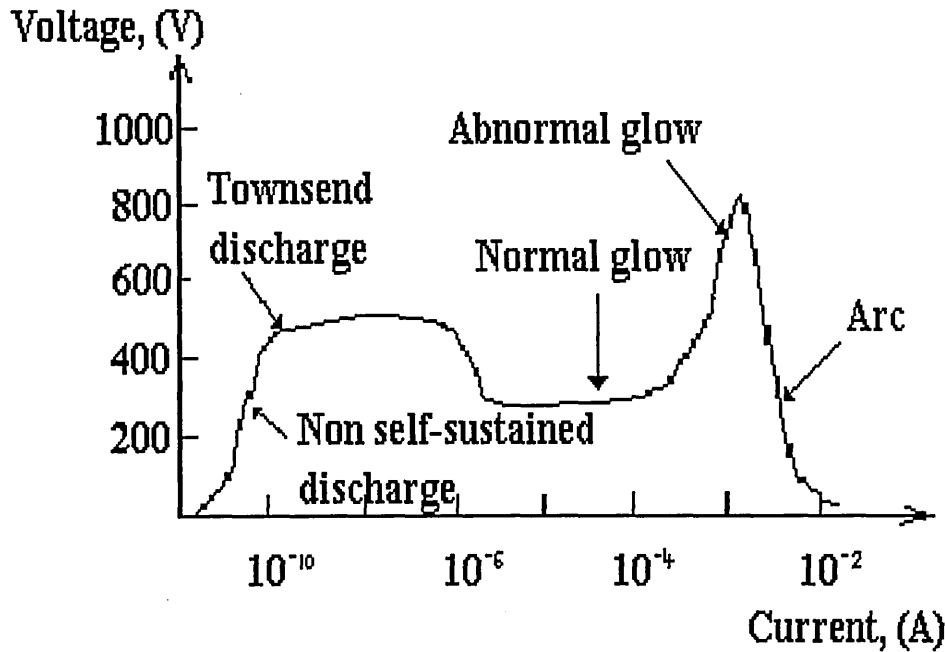


**Fig 2.4 Diode glow discharge procedure: voltage/current relation**

It is noted that for a low current there is insufficient ionisation to sustain the discharge unless external energy is applied. This region is known as the “non self-sustained discharge”. When the applied inter-electrode voltage (V) is increased, the discharge can become self-sustaining if the electrons emitted from the cathode have enough energy to produce further ionisation: this region is known as the Townsend discharge (15). In the region of the Townsend discharge, the electric field is more or less uniform between the cathode and anode due to the lack of appreciable space charge. If the applied power and hence discharge current is increased, the ions congregate close to the cathode to form a localised space charge which results in increased ion bombardment of the cathode/target surface. As a result of this bombardment, secondary electron emission is increased resulting in a reduction in the voltage. This region is defined as the “normal glow discharge” which consists of several distinct regions, see fig 2.5.

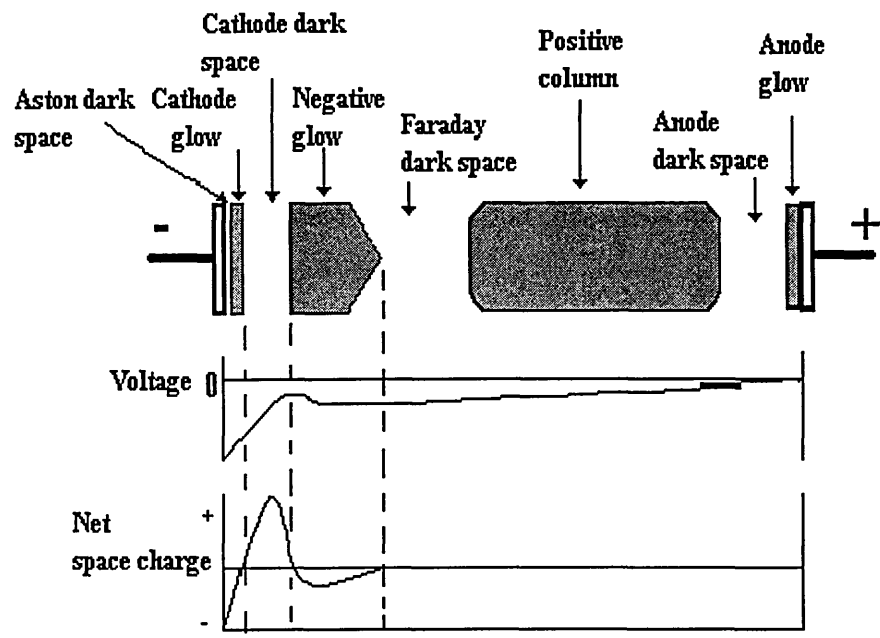


**Fig 2.5 Physical regions in glow discharge**

For the normal glow discharge, the region next to the cathode is the Aston dark space where the electrons leaving the cathode have insufficient energy to cause excitation. Adjacent to this is the highly luminous cathode glow region caused by neutralisation of the positive and negative ions. Beyond the cathode glow region is the cathode dark space or “cathode sheath” region. Most of the voltage is dropped across this region to provide the accelerating force necessary to drive the positively charged ions to the cathode. The dark space is formed due to plasma interactions with an electrically- isolated surface. Initially, due to higher random velocities the electron flux is greater than the positive ion flux, causing the surface to acquire a negative potential with respect to the plasma. Consequently an enhanced electric field is created which increases the positive ion flux at the surface. The thickness of this region is approximately the mean distance travelled by a secondary electron before an ionisation collision occurs. These secondary electrons produced by ion bombardment are accelerated across the cathode dark space until they enter a region where they have sufficient energy to cause ionisation and excitation of argon neutral atoms which helps to sustain the discharge. Relaxation and de-excitation events produce photons of wavelengths which are characteristic of the elements present. This is known as the negative glow region. The electrons eventually lose most of their energy until they can no longer produce further ionisation, causing the electrons to

accumulate in this region forming a slightly negative space charge. Beyond this region are the Faraday dark space, positive column, anode dark space and anode glow. However for sputtering plasmas it is not necessary to consider regions beyond the negative glow.

In a normal glow discharge using argon, the thickness of the cathode dark space is 0.3 torr centimetre and is independent of discharge current (16). In this state, all of the cathode area is not covered by the glow, as the current density is too low for the required sputtering rate, and the potential is too low to produce a high sputtering yield. If the power is increased, the glow eventually covers all of the cathode area and the current density increases with voltage. This state is termed the "abnormal glow".

Most sputter PVD systems use the abnormal glow discharge (17), as an increase in power sharply increases the voltage resulting in an increase in the target area carrying current and a more efficient deposition process. If the voltage is increased further, the current density rises and accelerates the ions with enough energy to cause thermal emission of electrons from the cathode accompanied by a large drop in voltage. This state is termed the arc discharge and will not be discussed further.

## 2.2 4. D.C. diode sputtering

The direct current (d.c.) diode sputter deposition arrangement is the simplest sputtering technique (18) and is shown schematically in Figure 2.6.

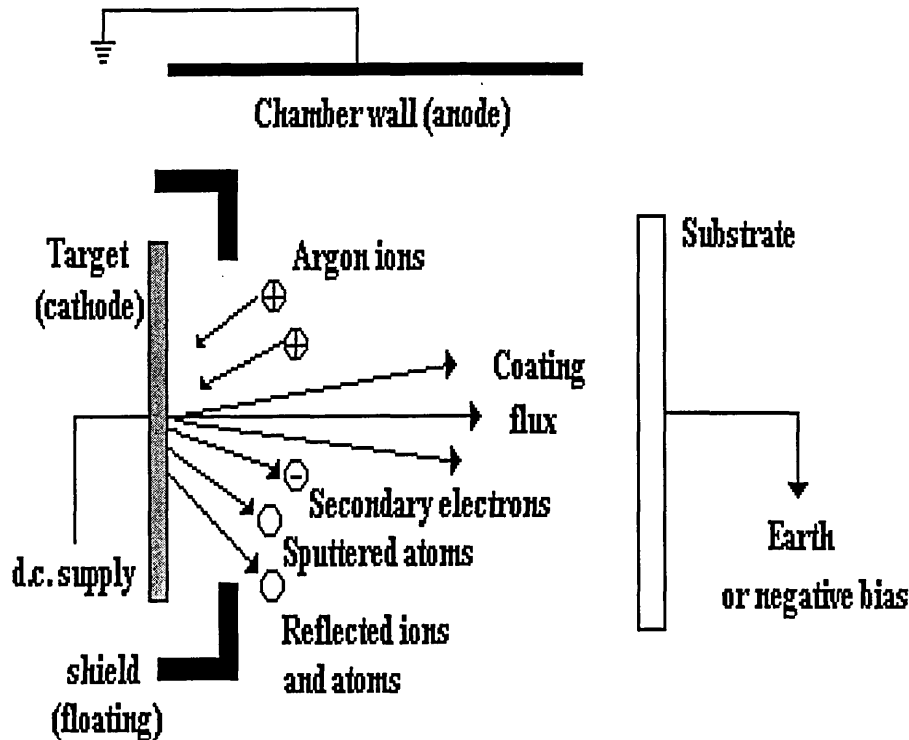


Fig. 2.6 d.c. diode schematic

The discharge is produced by introducing an inert working gas (normally Ar) into a vacuum chamber and applying a potential of between  $\sim 300$ - $5000$ V between two electrodes.

The naturally ionised portion of the gas is accelerated across the dark space towards the negative electrode (cathode). Most of the kinetic incident energy of the ions, on collision with the target, is lost in the form of heat. They also lose their charge and can either be elastically recoiled or implanted. A fraction of the energy ( $\sim 1\%$ ) (19), is transferred to the atoms near the surface of the target by momentum exchange. This momentum exchange creates collision cascades within the target which can result in the sputtering of surface

atoms. In addition to these target atoms, the substrate is also bombarded with charged particles, energetic ions (up to 30eV) and electrons (20). The majority of these electrons will be from the glow where they have energies of only a few electron volts (21), although only the most energetic will be able to surmount the substrate sheath. In addition to these slow moving electrons, the substrate is also bombarded with electrons emitted from the target resulting from the impact from ions and other particles which have been accelerated across the target dark space with energies in the range 100-1000eV. These “secondary electrons”, help to sustain the discharge as they are accelerated towards the grounded walls of the chamber and cause further ionisation, dissociation and excitation of the atoms and molecules present.

The number of secondary electrons emitted per incident ion is termed the “secondary electron yield”. For a sputtering process using Ar as the working gas and a pure metal target, this value is typically 0.1(22). In order for the discharge to be self-sustained, it must be operated at high pressure, typically >1 Pa, using a target voltage >1000V. High pressure is required due to the low mass of electrons which are consequently easily accelerated and therefore the electron mean free path tends to exceed the dimensions of the vacuum chamber. As a result of this the probability of further ionisation approaches zero at lower pressures. The d.c. diode sputtering arrangement is therefore inefficient. A number of modifications to the arrangement have been developed to improve this efficiency including the addition of an additional electron source such as a hot filament. For a full review of these aspects the reader is referred to D.S. Rickerby and A. Matthews, “Advanced Surface Coatings: A Handbook of Surface Engineering” (22). However, the only method to be discussed in this review is magnetron sputtering.

### 2.2.5. Magnetron sputtering deposition

The efficiency of the sputtering technique has been increased further with the use of a magnetic arrangement known as the “magnetron”. The effect of a magnetic field on a glow discharge was first discovered by F.M. Penning in 1936 (23). However it was not

until the 1970`s that this discovery was used practically in PVD sputtering systems for the deposition of metal and composite films (24,25,26,27).

The magnetron consists of a permanent magnet arrangement positioned behind the target, as shown by figure 2.7. The field lines extend into the dark space in front of the target and produce a magnetic field parallel to the target and an electric field perpendicular.

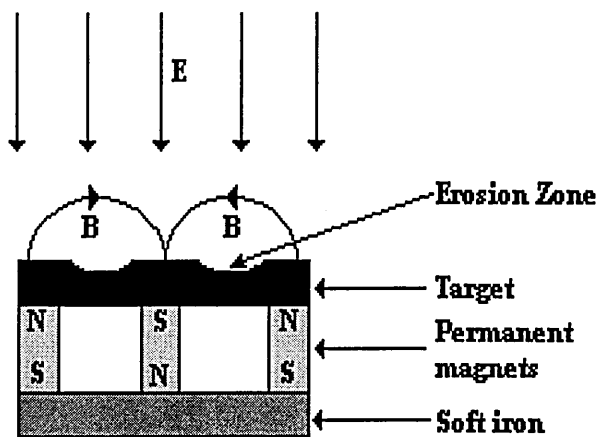


**Figure. 2.7** Cross-section of the magnetron cathode

This results in a force  $F$  being applied to a particle of charge  $q$  and velocity  $v$  perpendicular to both the magnetic field and the velocity. This may be expressed as

$$F = q\mathbf{V} \times \mathbf{B}$$

.....equation 2.4

Due to their low mass, this force significantly affects the movement of the electrons. The electrons that are not moving parallel to the magnetic field are subjected to a force  $eV\sin\theta$ , where  $\theta$  is the angle between the direction of the electron motion and the magnetic field, perpendicular to the lines of magnetic force, which traps the energetic secondary electrons in a region close to the target surface. In addition to this force, the electron motion is coupled with a velocity  $V\cos\theta$  parallel to the magnetic field. The resultant motion is therefore cycloidal around the magnetic field lines with a radius  $r$  given by the equation:

$$r = \frac{m_e V \sin \theta}{Be} \quad \text{.....equation 2.5}$$

As the electrons travel a longer distance before escaping the glow discharge through collisions, the ionisation probability is increased and hence so is the sputtering rate. For excellent reviews of the technique the reader is referred to Waits (28) and Thornton (29).

Magnetron sputtering offers distinct advantages over conventional diode and triode techniques, such as, higher deposition rate, and reduced substrate heating due to the confinement of the energetic electrons to the region close to the target.

Many magnetron configurations are available, such as cylindrical magnetrons (30), S-guns (31) and hollow cathodes (32). However the rectangular planar magnetron (33) is the most often used for practical applications as shown by figure 2.8.

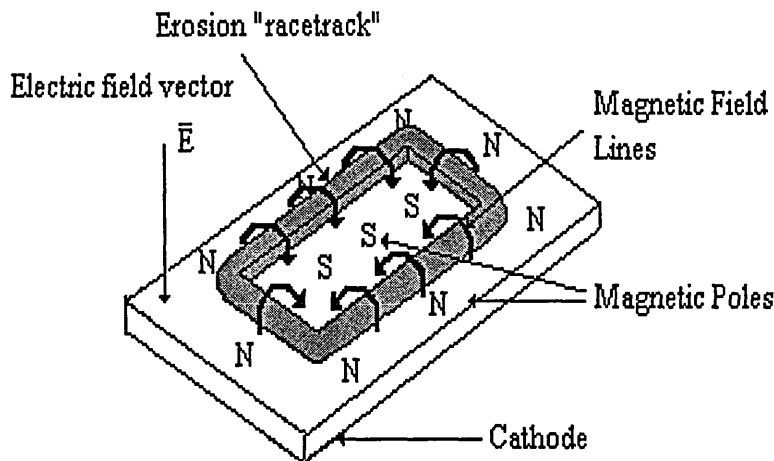


**Figure 2.8 Schematic of the planar magnetron cathode**

The magnetic field traps the glow to a region between the inner and outer magnetic poles, causing target erosion in the form of an ellipsoid “racetrack” on the surface.

As mentioned the conventional magnetron has many advantages over the diode and triode arrangements, however intrinsic problems still exist. The degree of ionisation and therefore the level of ion bombardment, falls rapidly with increasing target to substrate distance (34). The low level of ion bombardment results in less dense films with voids observed along grain boundaries (35). The ion bombardment can be increased by using a higher bias voltage. However, this may result in the generation of defects and hence poor quality films (36). Other problems include low ion bombardment and shadowing of three dimensional substrates (37), and inefficient use of the target due to the localised erosion area (38). Recently, however many of the deficiencies of the magnetron have been eliminated with the development of the “unbalanced magnetron” system.

## 2.2.6 Unbalanced Magnetron

Window and co-workers first introduced the concept of the unbalanced magnetron (39, 40, 41) in 1986. In an ideal balanced system with conventional magnetron, the inner and outer poles of the magnets behind the targets are equal in strength. The field lines loop between them as shown by figure 2.9a returning via the steel yoke on which the magnets are fixed. By increasing the strength of the inner or outer set of magnets, the magnetron becomes unbalanced as shown by figure 2.9b.

To maximise this unbalancing effect to improve the coating process the outer poles are strengthened (42). This causes the magnetic field lines to curve away on all sides, as well as looping on the cathode surface. Some of the secondary electrons follow helical paths along these field lines and are no longer confined to the cathode surface.

The glow is also expanded away from the surface of the target towards the substrate due to the need to maintain electrical neutrality within the plasma (43). This considerably increased the intensity of substrate ion bombardment to a value comparable with other high deposition rate techniques. Even at low bias potential, the technique provides ratios of ion to deposited atoms of up to 2:1. By changing the strength of these outer magnets the "*degree of unbalance*" can be altered and therefore the bias current density can be adjusted independent of the discharge voltage or discharge power. This makes it possible, within certain limits, to adapt the bias current density to the required coating properties and to the maximum temperature at a pre-selected bias voltage.

There are, though, limitations to the technique. An unwanted side effect is that by changing the strength of the magnetic field the used area of the target changes. When the outer poles are strengthened, the used target area decreases accordingly. Another problem is that the substrate current density decreases rapidly with distance from the centre of the target towards the outer edge (44). Sputtering is also a line of sight process which can result in shadowing of three-dimensional substrates and therefore porous structures and low quality coatings can result (45).

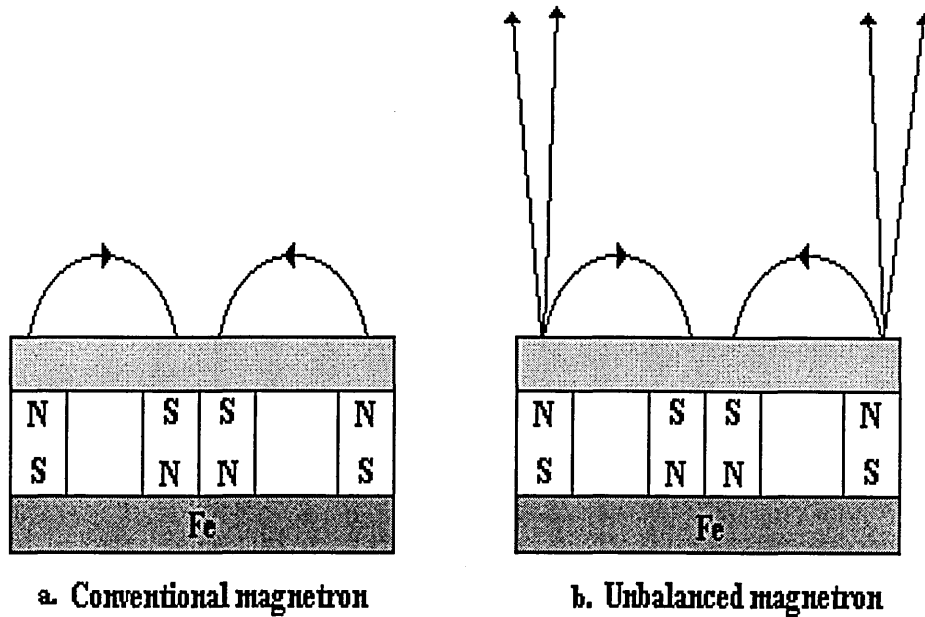


Figure 2.9 Magnetron configurations

### 2.2.7 Closed-Field Systems

Plasma confinement and density polarisation within a vacuum chamber can be affected by the arrangement of a pair of magnetrons. The two configurations which are generally possible are:

(i) Mirrored, where like poles face each other as shown by figure 2.10a. This arrangement reduces the degree of unbalancing by restricting the reach of the uncontained field lines to half the inter-cathode distance.

As a result electrons follow the field lines and are lost to the chamber walls. Research has shown that such an arrangement produces a low plasma density at the substrate and at times the observed substrate bias current densities were less than  $1\text{mA}/\text{cm}^2$  (48). The hard coatings produced using the mirrored configuration have been generally of low

quality with poor adhesion caused by the low plasma density and etching problems at the substrate.

(ii) Closed field (46,47), where opposite poles face each other, as shown by figure 2.10b. In this case even numbers of cathodes are used in an opposed arrangement. This configuration causes field linking between the north and south outer poles of adjacent cathodes (48).

This prevents the secondary electrons from escaping and distributes them, along with the plasma, around the multi-cathode system. Changes in deposition conditions are also possible as the closed magnetic field confines the plasma to the substrate region.

As a result of the increased travelling distance of the secondary electrons in front of the cathodes, more ionisation events occur with a resulting increase in sputtering. The development of multi-cathode units using unbalanced closed field geometry has generally solved the problems observed in single cathode systems (49, 50).

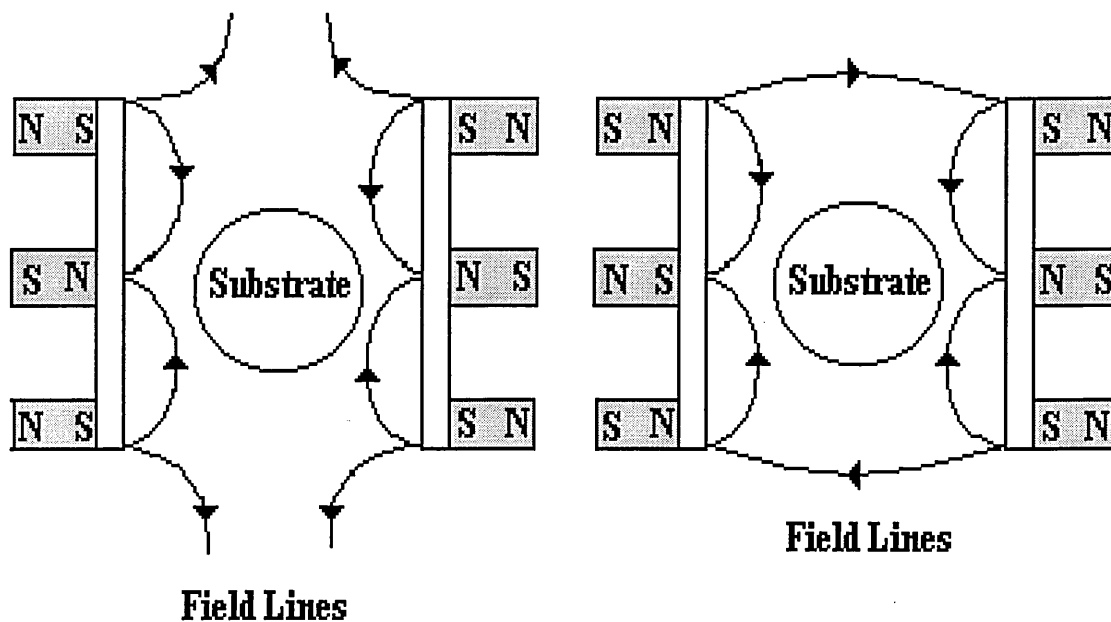


Figure 2.10 Schematic of the mirrored and closed-field arrangements

## 2.3 Coating Deposition, Structure and Properties

### 2.3.1 Film Growth

In the PVD coating process, the sputtered material upon reaching the substrate condenses from the vapour to form the solid phase. The subsequent film growth can be described as a four stage process (51): nucleation, island growth, coalescence, and continuous growth.

In stage 1, nucleation, the incident atoms become adatoms on the substrate surface where they lose excess energy that would enable them to escape the surface potential barrier, ( $W$ ). A polycrystalline substrate surface possesses many defects such as dislocations, monatomic steps, vacancies, and adatoms where the probability of nucleation is higher due to localised changes in the electronic states of the surface, and a lack of adjacent neighbouring atoms which results in chemical bonds available for possible reaction (52). When the adatoms meet such defects the probability of formation of more stable aggregates or clusters forming is increased.

Once nucleation sites have been established “island” growth takes place. The clusters begin to grow both vertically and laterally across the surface area, stage 2, until they meet other islands and coalesce. Once this happens a grain boundary defect is generated and growth continues in the vertical direction alone.

In the third stage, most of the substrate surface is covered by growing islands. Each island grain will initially be orientated to match, as nearly as possible, the orientation of the underlying surface grain at the absorption site. However, competitive growth occurs, where grains with a particular orientation take preference and grow at the expense of adjacent grains orientated differently. This occurs due to the incident ion energy, gas pressure (53, 54) and surface and strain energy minimisation for different crystallographic planes (55,56,57,58,59,60). As the film thickens, the columns cluster together to form larger features with preferred orientation, and produce a columnar structure (61). The early growth of PVD films can be classified into three mechanisms (62).

- (i) Layer-by-layer growth (Frank-van-der-Merwe) where the binding energy of the film, ( $E_f$ ), is equal or less than that between the film and substrate, ( $E_{f-s}$ ) and the strain energy of the film is small compared to the surface energy.
- (ii) Combined layer-by-layer with three dimensional island growth (Stranski-Krastanov) where  $E_f$  is lower than  $E_{f-s}$  and the strain energy in the film is large in comparison to the surface energy.
- (iii) Three dimensional island growth (Volmer-Weber) where  $E_f$  is larger than  $E_{f-s}$  which results in immediate nucleation on the surface.

### 2.3.2 The microstructures of the sputter deposited film

A wide range of microstructures is possible for sputter deposited films. These are dependent on the deposition conditions and range from a porous, open structure to re-crystallised densely packed columns. Movchan and Demchishin (63) first classified these structures as a function of the substrate temperature divided by the coating material melting point. They identified a low-temperature, zone 1 structure which consisted of widely spaced columns with domed tops which formed due to low adatom mobility. A mid-temperature zone 2 structure was identified where surface diffusion becomes a significant factor and this consists of densely packed columns with a smooth surface. For Zone 3, the high temperature region, bulk diffusion becomes predominant and the structure becomes equiaxed. Later work by Thornton (64) took account of the influence of working gas pressure. As can be seen from the Thornton diagram (Figure 2.11) a further region, (Zone T) is observed between zones 1 and 2 consisting of densely packed fibrous grains.

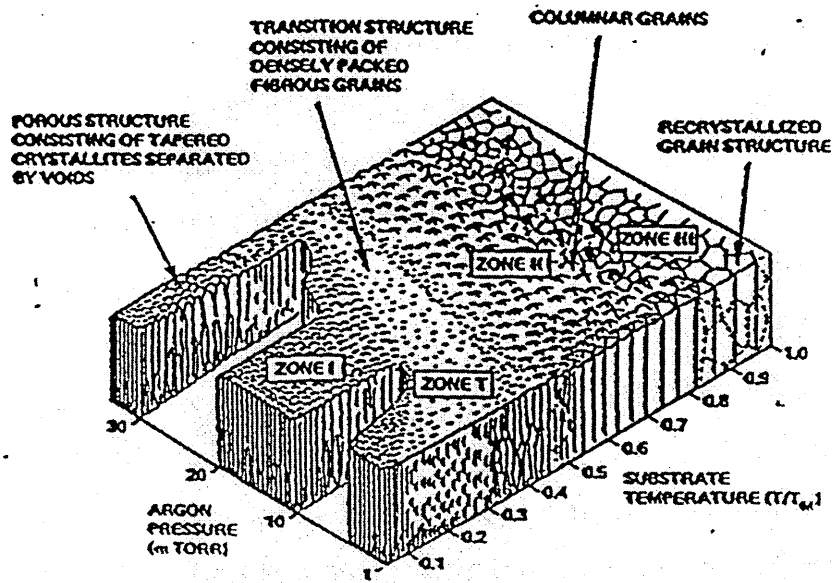


Figure 2.11. Thornton Zone Model

The latest structure zone model was developed by Messier (65) and shows how when a substrate bias voltage is applied, high energy ion bombardment during growth results in denser films due to increased adatom mobility.

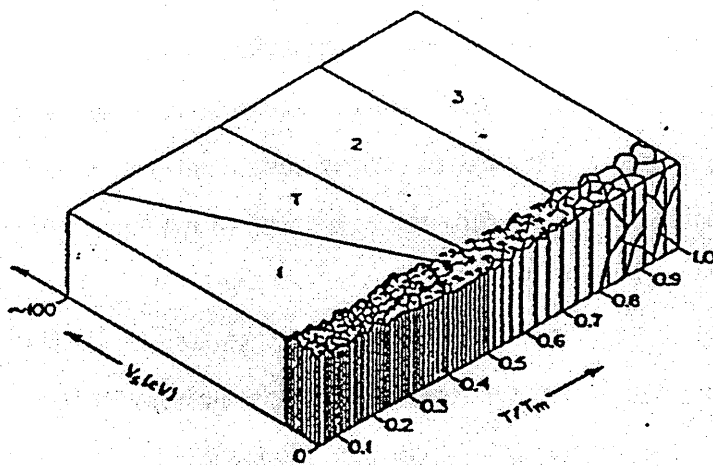


Figure 2.12 Messier Structure Zone Model

### 2.3.3 Ar<sup>+</sup> Sputter Etching

Before deposition, impurities must be removed from the surface of the substrate to improve the quality of the resultant coating. These impurities include thin oxide layers, other chemically bonded molecules, water vapour, etc. To this end the substrate is cleaned using an argon glow discharge. At an argon pressure of  $\sim 2.5 \times 10^{-3}$  mbar a weak plasma is established by applying a potential of 200V to each target which results in secondary electron emission to sustain the discharge. A substrate bias of -1200V is then applied which causes the substrate to behave like a cathode in a d.c. discharge. When the accelerated Ar ions impinge on the substrate surface they lose their kinetic energy by transfer of momentum to the surface atoms. This results in, amongst other effects, the removal of surface atoms and the cleaning of the surface for deposition.

### 2.3.4 Crystallographic Texture

A feature often observed when depositing PVD films is a pronounced preferred orientation, i.e. the film is growing with one particular crystal plane facing the vapour flux. The preferred orientation is generally the most densely packed plane e.g. the (110) plane for a bcc crystal. However, it is, among other features, dependent on the anisotropy in the surface energy for different crystallographic planes and other features. Monte Carlo simulations (66) have shown that even if the initial film nucleation results in randomly oriented grains, the film will quite rapidly transform to an orientation with the lowest surface energy during growth. It has also been reported recently by several workers (67,68,69,70,71), that the texture of a coating can change due to the competition of two orientation-dependent driving forces: surface energy minimisation and strain energy minimisation. These do not favour the growth of the same orientations and compete to determine the orientation and microstructure of the film.

In order to obtain the texture coefficients ( $P$ ), the normalised intensities are divided by the average of all the normalised intensities, according to the following equation, (72).

$$P = \frac{I_{(hkl)} / R_{(hkl)}}{(1/n) \sum_0^n I_{(hkl)} / R_{(hkl)}} \quad \text{.....equation 2.6}$$

where,  $I_{(hkl)}$  is the measured integrated intensity of a given (hkl) reflection in the sample,  $R_{(hkl)}$  is the calculated theoretical intensity for the same (hkl) reflection in a randomly orientated specimen and  $n$  is the total number of reflections from the random specimen in the examined range of  $2\theta$ . The texture coefficients, calculated from the above equation, are proportional to the diffracting volume in the given orientation and a 'P' value of unity indicates random orientation while values greater than unity indicate preferred orientation. The summation is over all  $n$  independent measured reflections and  $R_{hkl}$  are the theoretical intensities (including structure, polarisation, Lorentz, absorption, and multiplicity factors). The full equation for the calculation of the theoretical intensities is shown in appendix 1.

### 2.3.5 Residual Stress

Compressive residual stress is present in virtually all PVD deposited coatings. It is an important factor as it influences the coating adhesion, the maximum coating thickness allowed before spallation (73) and the hardness of the film. The level of stress in the film is a combination of two components: thermal stress and intrinsic stress. Thermal stress results from a mismatch in the thermal expansion coefficients of the coating and substrate lattices, and can be calculated using;

$$\sigma = \frac{E\Delta\alpha\Delta T}{1-\nu} \quad \text{.....equation 2.7}$$

where  $E$  is the Young's modulus of the coating,  $\Delta\alpha$  is the difference in the thermal expansion coefficients,  $\Delta T$  is the difference between room and deposition temperature and  $\nu$  is the Poisson's ratio of the coating.

The intrinsic stress in a coating is to varying degrees associated with a number of deposition conditions and coating features including (74):

- Incorporation of residual gas and impurity atoms in the coating lattice
- Grain size, microvoid, and dislocation density in the coating
- Energetic particle bombardment during deposition
- Combination of surface tension and growth process at grain boundaries

Although many phenomenological models have been proposed to explain intrinsic stress, a generalised model for various coating materials and deposition processes is unlikely at this time due to the limited information regarding associated structural details.

### **2.3.6 Grain Growth Driving Mechanisms**

Grain growth can occur during deposition of thin films or during post-deposition processing. It not only results in a dramatic increase in the average crystal size in a film but can also result in changes in the average crystal orientation.

Grain growth in thin films is fundamentally different from grain growth in bulk materials. One of the main reasons is that the interface of the film with the substrate together with the top surface of the film play important roles in suppressing normal grain growth and promoting abnormal grain growth. Due to the anisotropic nature of the surface/interface energy, secondary grains generally have restricted crystallographic orientations and increased size. For an extensive review of the mechanisms and modes of grain growth in thin films the reader is referred to the work edited by G. Abruzzese and P. Brozzo (75).

Further work (76,77) has shown that the texture of a coating can change due to two, orientation dependent, driving forces: surface energy minimisation and strain energy minimisation. These do not favour the growth of the same orientations and compete to determine the orientation and microstructure of the film. Both factors play an important role in texture evolution in thin films and should be considered in understanding experimental results and in the development of models for grain growth in thin films. Which energy minimisation process is most important will be a strong function of a

deposition temperature relative to the grain growth temperature, as well as the film thickness. It is argued that there will always be a film thickness below which surface-energy minimisation will control grain growth while at high stresses, strain-energy minimisation can lead to other textures.

### 2.3.7 Solid Solutions

The incorporation of impurity atoms into a crystal lattice distorts the lattice and generates stress in many cases. Compounds or inter-metallic phases can be formed but in most cases if the level of impurity is low solid solutions are formed. Solid solutions are homogeneous mixtures of two or more atoms in the solid state. They are usually crystalline, with the more abundant atomic species termed the solvent, the less abundant, the solute. There are two distinct types, *substitutional* and *interstitial*. In the former a direct substitution occurs between solute and solvent atoms, whereas in the latter the solute atom enters one of the holes between the solvent atoms, both types are illustrated schematically in figs 2.13a and b.

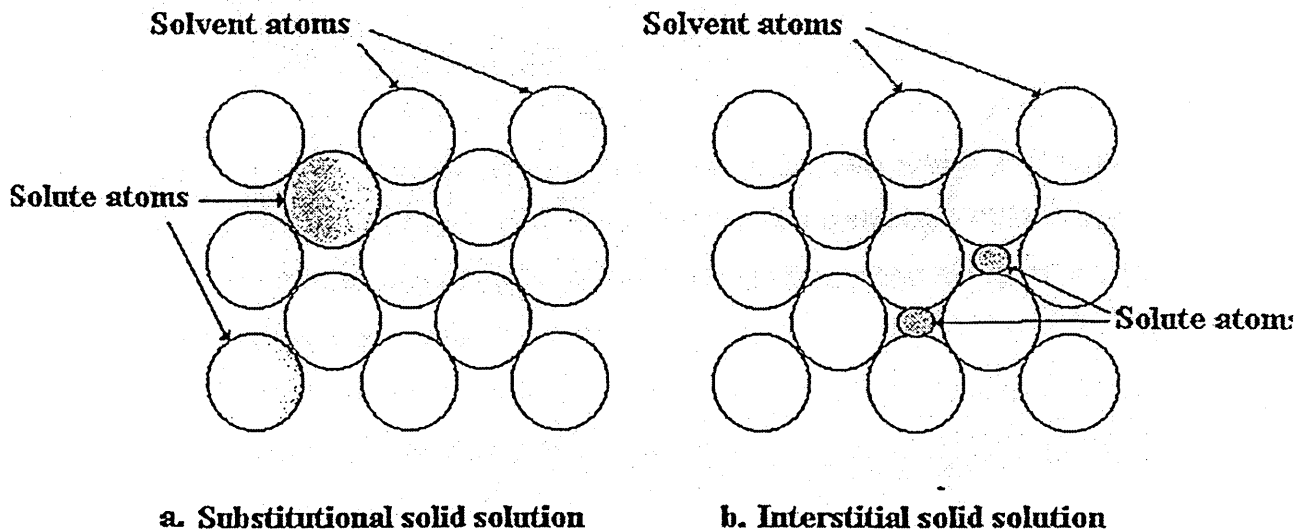


Figure 2.13 Substitutional and interstitial solid solutions

For the materials system used in this investigation, only substitutional solid solutions are formed because the Cr atoms are too large to fit into interstitial sites. For a full review the reader is referred to “Physical Metallurgy Principles” 3rd edition by R.E. Reed-Hill and R. Abbaschian (78).

An important factor governing solution behaviour is the relative size of the atoms. A continuous series of solid solutions is found only between elements of the same crystal structure and only when the sizes of the atoms differ by less than 15 per cent (80).

Usually the lattice of an element is expanded by dissolving atoms larger than those of the solvent and contracted by dissolving atoms smaller than those of the solvent. The law of linearity between lattice spacing and solute atomic percent, Vegard’s (79) law, was discovered with solid solutions, which are ionic crystals. When applied to metallic systems there are almost invariably deviations from the law which can be either positive or negative (80).

### **2.3.8 Cross-contamination**

An extensive literature search found no published work on the existence of cross-contamination in PVD systems. However, the use of a multitarget PVD system without individual shutters, to provide multilayer coatings raises the question of potential cross-contamination between atoms from targets of different metals. During a typical process using the Hauzer HTC 1000-4 ABS™ system targets which may need to be used only in the etch stage are given a negative applied voltage, nominally, between -200 to -250V. The applied voltage causes sputtering of coating material with the aim to prevent overall deposition of unwanted coating material onto the unused targets.

This study aimed primarily to determine whether potentials of this magnitude are sufficient to cause sputtering of the target material and therefore cross-contamination in the resulting coating. The secondary aim was to identify any correlation between mechanical

performance and levels of chromium in niobium coatings due to the chromium target voltage.

## 2.4 Coating Materials

This study is concerned with Niobium-Chromium coatings. Commercially pure Niobium, also known as Columbium, is ductile and easy to fabricate. It is a group five element and therefore has five valence electrons available. It is very resistant to chemical attack from most organic and mineral acids below 100°C although it is attacked by HF, and its resistance to alkali attack is poor. The main disadvantage of Nb is high cost, hence the development of thin films on suitable substrates is attractive.

### Niobium-Chromium, (Nb-Cr) System

The atomic radius of niobium, (1.46 Å) (83) is much larger than that of chromium, (1.256 Å) (83) and therefore the solution of chromium in niobium contracts the lattice parameter of the latter. For example, the lattice spacing of Nb,  $a = 3.3062 \text{ \AA}$ , changes to  $a = 3.255 \text{ \AA}$  at the solid solubility limit at 1550°C (about 9 at. % Cr) Eljutin and Funke(80, 81) report that Nb dissolves about 12.5 at % Cr at 1500 C, with  $a = 3.29 \text{ \AA}$  at 10 at. % Cr, and  $a = 3.26 \text{ \AA}$  in a two phase alloy with 20 at. % Cr. It can be seen from the binary phase diagram, (Figure 2.14) (82), that as the temperature is lowered the solubility of chromium decreases.

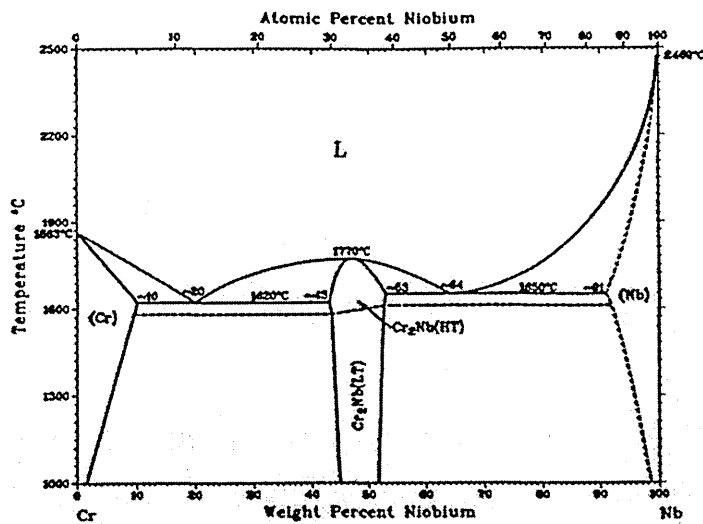


Figure 2.14. Binary Phase diagram of Nb-Cr

## 2.5 Coating Performance

### 2.5.1 Corrosion Resistance

Niobium coatings can be used in applications where protection is needed from aqueous corrosion (83), hot gas erosion (84), or liquid metal corrosion (85). Due to difficulty in depositing niobium coatings by so-called conventional methods, the coatings are normally deposited using physical vapour deposition. However, niobium coatings deposited at low temperature usually consist of columnar grains with open boundaries which impair coating performance. One method to improve the density is to concurrently bombard the surface with ions during deposition (86,87). Another method, which has been shown to improve the coating structure and density of niobium, is to codeposit with chromium (88,84,89). J.H. Hsieh (88) produced Nb-Cr alloy coatings using ion beam-assisted deposition and found the Nb-30%Cr alloy coating to be the most corrosion resistant, probably because it readily forms a niobium enriched oxide layer at the surface. It is generally believed that Nb-Cr alloy coatings are corrosion protective if a niobium enriched oxide film is formed at the surface (88). However, as this work investigates the

problem of cross-contamination, the level of Chromium in the deposited coatings is much less, typically <8 atomic %.

### **2.5.2 Friction and Wear**

For a full review of the theories of wear and friction the reader is referred to Tribology by I.M. Hutchings (90). No work on the investigation of the wear of Niobium coatings was found in the literature.

### **2.5.3 Microhardness**

With reference to the mechanisms of solid solution strengthening, as the atomic size of Cr (1.256 Å) (83), is significantly different to Nb (1.46 Å) (83), the alloying element causes considerable elastic distortions in the crystal lattice which induce residual stress and dislocations which impede plastic flow. Such strengthening is observed at temperatures below  $0.5 T_m$  where the strengthening processes do not depend on the diffusion of alloying elements.

The literature values for the microhardness of the solid solution of Chromium in Niobium indicate it increases from 4.9 GPa for Niobium to 7.2 GPa for alloys containing 80 atomic % Chromium (83).

## Chapter 3

### 3. Experimental Details

#### 3.1. Experimental Design

The primary objective of this work, was to determine whether cross-contamination between targets of different metals, due to the lack of individual target shutters, significantly affects the mechanical performance of PVD coatings.

The equipment used to deposit the coatings was the Hauzer HTC 1000-4 ABS<sup>TM</sup>. For certain coatings the substrates are cleaned by arc evaporation using targets which may not be required for the subsequent coating. This system does not possess individual target shutters and therefore a negative voltage is applied to the unused targets during coating to sputter any unwanted coating material. Nominally, the voltage applied to 'unused' targets to prevent coating is set between -200 to -250V. This investigation looked at whether target voltages in this range caused sputtering and hence deposition of unwanted target material. A series of coatings were deposited with different negative voltages applied to the Cr target whilst depositing with Nb to determine the dependence of coating properties on levels of Cr cross-contamination in Nb coatings. In the event of such a dependence, further work may provide a more fundamental understanding of associated structure-property relationships and provide an insight into appropriate methods of control.

The elemental composition and crystalline structure of the resultant coatings were analysed respectively using Glow Discharge Optical Emission Spectroscopy (GDOES) and X-Ray Diffraction (XRD). The physical properties were analysed by corrosion, adhesion, universal hardness and wear tests

### 3.2. Sample Preparation for Coating

The following substrates were used in this investigation:-

- M2 high speed steel (HSS) discs ( $\text{Ø}30\text{mm} \times 10\text{mm}$ ) mechanically polished to a  $1\mu\text{m}$  diamond finish.
- Annealed stainless steel rectangular sheet ( $25\text{mm} \times 25\text{mm} \times 1.5\text{mm}$ )

The substrates were cleaned according to the following procedure:-

1. Degreased in an alkaline solution at  $70^\circ\text{C}$  for 3 minutes in an ultrasound bath.
2. Rinsed in tap water.
3. Degreased in an alkaline solution at  $70^\circ\text{C}$  for 3 minutes in an ultrasound bath.
4. Rinsed in distilled water.
5. Rinsed in distilled water for 2 minutes in an ultrasound bath.
6. Finally rinsed in distilled water for one minute.
7. Hot-air dried

### 3.3 Process Details

Nb-Cr coatings were co-sputter deposited using a Nb target power of 8kW and Cr target voltages between 0 and 350V in increments of 50 volts. Figure 3.1 shows a cross-section of the vacuum chamber showing the 2 targets used during deposition. The process details are given in table 3.1.

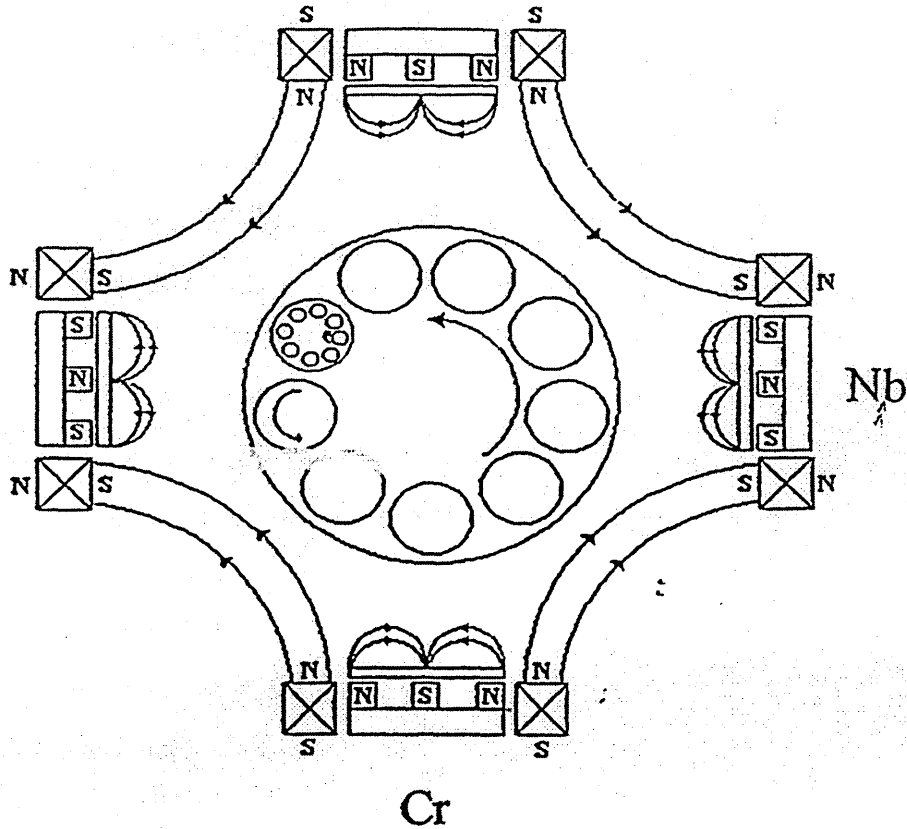


Figure 3.1. Cross-section of the vacuum chamber showing the Nb and Cr targets.

**1. Pump down and chamber heating**

Base pressure,  $3 \times 10^{-5}$  mbar Temperature (radiant heating), 390 °C

**2. Glow discharge target cleaning, exposure time 10 mins.**

Shutters directly in front of targets.

Power to each target, 5kW, Argon flow, 220sccm

Working pressure,  $2.7 \times 10^{-3}$  mbar.

Substrate bias voltage, 0V.

Unbalancing coil current, 0A.

Temperature, 400 °C.

**3. Glow Discharge Ar ion etch, time 10 minutes.**

Arc current, 100A.

Substrate bias voltage, -1200V.

Substrate temperature, 400 °C.

Argon flow, 220sccm.

Working pressure,  $2.7 \times 10^{-3}$  mbar.

Coil current, 5A.

**4. Unbalanced magnetron metallic coating, Coating time 1 hour.**

Fixed magnet array moved away from targets

All targets in magnetron mode.

Power to Nb target 8kW.

Cr target voltage, 0, 50, 75, 100, 125, 150, 175, 200, 250, 300, 350V

(Each value corresponds to a different run)

Substrate bias voltage, -80V.

Temperature, 400 °C.

Working pressure,  $2.3 \times 10^{-3}$  mbar.

Argon flow, 220 sccm.

Unbalancing coil current, 6A per coil (closed field geometry).

**Table 3.1 Process Details**

### 3.3. Techniques used to characterise the coatings

#### 3.3.1. X-Ray Diffraction, (XRD)

All X-ray diffraction analysis was performed using a Philips PW1710 Powder diffractometer, using Cu K $\alpha$  x-radiation ( $\lambda = 1.542 \text{ \AA}$ ) and Bragg-Brentano geometry except for the glancing angle work which was carried out at Hull University using a Siemens D5000 X-ray diffractometer. A current of 40mA and a voltage of 40kV were used for both instruments. The techniques were used to determine the texture, degree of orientation, and lattice strain and normal scans to determine crystalline structure. For a full review of the theory of X-ray diffraction the reader should see Cullity (91), "Elements of X-ray Diffraction".

#### Crystallographic Texture

In order to obtain the texture coefficients  $P$ , the measured and normalised X-ray peak intensities were divided by the average of all the normalised intensities, according to equation 3.1(92).

$$P = \frac{I_{(hkl)} / R_{(hkl)}}{(1/n) \sum_0^n I_{(hkl)} / R_{(hkl)}} \quad \text{.....equation 3.1}$$

where,  $I_{(hkl)}$  is the measured integrated intensity of a given (hkl) reflection in the sample under examination and  $R_{(hkl)}$  is the calculated theoretical intensity (including structure, polarisation, Lorentz, absorption, and multiplicity factors) for the same (hkl) reflection in a randomly orientated specimen, (see appendix 1 for the theoretical intensity calculation). 'n' is the total number of reflections from the random specimen in the examined range of  $2\theta$ . The texture coefficients, calculated from the above equation, are proportional to the

diffracting volume in the given orientation, a  $P$  value of unity indicates random orientation whereas values greater than unity indicate a preferred orientation.

### **Omega Scan**

Due to the highly (110) textured nature of the coatings Omega scans were used to give an indication of the degree of orientation (93). The detector is set at the maximum intensities of the (110) and (220) reflections and then rocked around this point over an angular range of 0 to 37 degrees for the (110) reflection and 0 to 80 degrees for the (220) reflection.

The Full Width at Half Maximum, FWHM of the subsequent diffraction peak indicates the degree of orientation, for a full description of the technique the reader is referred to a review of X-Ray Diffraction methods by B.D. Cullity (93).

### **Asymmetric Bragg-Brentano Stress Analysis**

This method enabled a measure of the biaxial stress in the samples. The method is applicable for polycrystalline films where the reflections from the substrate do not interfere with the film reflections and details of the theory and interpretation of the residual stress measurements are well described in the article "Stress Determination for Coatings" in volume 5 of the *ASM Handbook* (94).

In the " $\sin^2\phi$  method", strain is evaluated by measuring interplanar spacings,  $d_{hkl}$ , as a function of the inclination angle  $\phi$ , which is defined as the angle between the (hkl) planes and the sample surface. In the linear plot of  $d^{hkl}$  vs  $\sin^2\phi$ , the intercept is  $I = d_n$ , the lattice spacing of the plane normal to the surface, and the gradient,  $M = \sigma d_n [(1 + \nu^{hkl}) / E^{hkl}]$ , where  $\sigma$  is the stress, and  $d_n$  is the lattice parameter normal to the substrate surface. The stress of the coating can then be calculated using equation 3.2 if the Young's modulus  $E$  and Poisson ratio values,  $\nu$ , are known for the particular material.

$$\sigma = M / \{d_0[(1+\nu^{hkl}) / E^{hkl}]\} \quad \text{.....equation 3.2}$$

The peak positions and the associated d values were obtained using Philips PC-APD X-ray diffraction software and the stress measurements were performed on the higher order (220) Nb reflection as the  $\varphi$  angle is limited by  $2\theta$ .

### **Glancing Angle X-Ray Diffraction, (GAXRD)**

An alternative method of stress analysis is glancing angle X-ray diffraction, (GAXRD). In the “ $\sin^2\varphi$  method”, a single peak is used and the variation in the value of the angle  $\varphi$  also affects the penetration depth of the incident beam and as a result, any stress gradient through the coating affects the result, see A.J. Perry (95) for further details. In the Glancing Angle X-ray Diffraction method, all peaks within the instrumentally permitted range are used and diffraction occurs at a given, near constant depth of penetration.

The angle of incidence  $\gamma$  is set, in this case values of 1 and 3 degrees were used. These angles were chosen to give an indication of the stress near the surface of the coating and the stress near the substrate/coating interface after using the Siemens D5000 X-ray diffractometer software to determine the X-ray depth of penetration. The diffraction angle is now given as  $\theta - \gamma$  and a plot of lattice spacing vs.  $\sin^2(\theta - \gamma)$  has slope and intercept as the previous method using Bragg-Brentano geometry, hence a measure of the stress in the sample can be calculated using different incident angles if the elastic constants for the material are known.

### **Line broadening analysis**

When diffraction peaks are broadened there are, generally, two major causes: non-uniform strain and/or small crystallite size (96). Strain effects are a function of diffraction angle while crystallite size affects all the line profiles equally. Broadening caused by stacking faults and inhomogeneity are also a function of diffraction angle. Separating the

broadening contribution due to strain and crystallite size effects can be done by methods such as the Gauss-Squared or Hall-Williamson methods (91). The quantitative precision of these methods is dependent on how well the diffraction peaks are profiled to give accurate peak widths as well as how efficiently instrumental broadening can be subtracted.

Due to the highly textured nature of the thin films analysed, the less-stringent Gauss method was chosen for this analysis (91). With the Gauss relationship:

$$(\beta \cos \theta / \lambda) = (1 / D_G) + 16e_G (\sin \theta / \lambda) \quad \text{.....equation 3.3}$$

where  $\beta$  is the broadening of the peak corrected for instrumental breadth,  $\theta$  is the diffraction angle and  $\lambda$  is the wavelength of the X-rays used ( $\text{CuK}\alpha_1=1.5406\text{\AA}$ ).  $D_G$  is the contribution to peak broadening from the grain size, and  $e_G$  is the contribution from the strain in the lattice. Thus from a linear plot of  $\beta \cos \theta / \lambda$  versus  $\sin \theta / \lambda$  the slope of the least squared line through the breadth function in each phase determines the strain ( $16e_G$ ) while the intercept is the crystallite size function ( $1/D_G$ ).

The presence of an upward influence on the gradient of the  $\beta \cos \theta / \lambda$  versus  $\sin \theta / \lambda$  indicate broadening due to stacking faults and/or inhomogeneity as they are a function of diffraction angle. If this is not the case, then the broadening is due to crystallite size differences.

### 3.3.2. Glow Discharge Optical Emission Spectroscopy, (GDOES)

A Leco GDS-750 glow discharge spectrometer was used for this study. The wall of the vacuum chamber acts as the anode and the sample itself as the cathode. After the chamber is evacuated and backfilled with argon, the cathodic sputtering process is created by applying a stable voltage to the sample. The surface atoms removed by the sputtering process diffuse into the plasma where excitation and emission occur. Upon relaxation to a lower energy level radiation quanta are emitted with characteristic wavelengths of the elements present. The glow discharge spectrometer uses a polychromator to separate the

spectral wavelengths for measurement by photomultiplier tubes. The intensities of the lines are proportional to the number of emitted quanta in the plasma, and hence to the elemental concentration within the sample. The technique gives a quantitative depth profile of the elements present in the sample. The accuracy of the method can be affected by factors such as nonuniform crater shape and surface roughness.

The system can be operated in constant current or voltage mode as both are functions of the emission line intensity, and quantification is performed against a range of standard reference materials of accurately known concentration.

### **3.3.3. Scanning Electron Microscopy, (SEM)**

Scanning electron microscopy (97) was used to view the surface morphology of the coatings. A Philips XL40 SEM was used in this study with a secondary electron detector to view the topography of the surface and a back-scattered electron detector to give atomic number contrast.

### **3.3.4. Corrosion Test**

Potentiodynamic polarisation measurements using an EG&G Galvanostat/Potentiostat 263A were carried out to determine the corrosion resistance of a series of the Nb-Cr alloy coatings. The measurement of the corrosion resistance is based on the formation of passive thin oxide films which act as a barrier to the anodic dissolution reaction. The chloride ions in the electrolytic solution initiate localised corrosion or pitting as the passive film is often very thin and fragile. This is followed by a steep increase in the current density, hence the level of corrosion resistance can be determined from the range in which passivity occurs and the anodic current density. For a full review of the theory of corrosion the reader is referred to D.A. Jones, "Principles and prevention of corrosion" (98). All samples were tested using a 3% NaCl solution and polished M2 high speed steel substrates, with a testing area of 0.78 cm<sup>2</sup> and the following test cycle:

1. A 55 minute aeration period.
2. Cathodic cleaning of the sample for 100 seconds at  $E = -1700 \text{ mV}$ .
3. 20-40 minute delay to stabilise the potential after cathodic cleaning.
4. Polarisation in the potential range of  $-800\text{mV}$  to  $+900\text{mV}$  at a scan rate of  $1\text{mVs}^{-1}$ .

Carbon electrodes were used with a saturated calomel electrode as a reference

### **3.3.5. Microhardness Test**

The technique recommended for coating thicknesses less than  $5 \mu\text{m}$  is the universal hardness HU test. It measures ultra-low load hardness under test load, based on penetration depth measurements during a loading and unloading cycle with specially shaped indentors. The method is based on the correlation between the indentation depth and the geometry of the indenter. The hardness value, HU is derived from the test load,  $F$  and the indentation surface area, which in turn is derived from the indentation depth,  $h$ . In a single test cycle information about surface hardness, elastic and plastic properties, and the creep behaviour of the material is collated, along with a hardness profile as a function of indentation depth in the layers close to the surface.

### **3.3.6. Rockwell Indentation Adhesion Test**

A qualitative statement about the adhesive strength and ductility of the coating is given by the Rockwell adhesion test (99).

Using a conventional Rockwell-C indentation test with a 150 kg load, a mechanically stable crack is introduced into the coating-substrate system. The resistance to propagation of the crack along the interface is then used as a measure of the adhesion. The sample surface must have a low roughness depth and the coating thickness must be less than  $4 \mu\text{m}$  and at least two measurements are necessary for good reproducibility.

Classification of the adhesion is determined by observation of the cracking or spallation of the coating using either optical or scanning electron microscopy. Depending on the extent of the failure the coating may be classified as either acceptable or not, but no specific adhesion value is normally assigned.

### **3.3.7 Friction Test**

Friction tests were carried out using a CSEM tribometer pin-on-disc wear and friction system consisting of a test module, a data acquisition unit and a computer-based chart recorder used to display data in real time. The test module consists of a turntable which holds the disks; the pin (a 100Cr6 steel ball) is attached to a precision-balanced lever arm which applies vertical loads to the pin and reads the frictional force on the pin via a force gauge. A constant, normal load of 1N and a sliding speed of  $1 \times 10^{-2} \text{ ms}^{-1}$  were used.

## Chapter 4

### 4. Results

#### 4.1. Glow Discharge Optical Emission Spectroscopy, GDOES

Figures 4.1-4.7 show the GDOES depth profiles for the series of Nb-Cr coatings with increasing Cr target voltage. Table 4.1 shows the atomic percentage of Cr at the interface of each coating and table 4.2 shows the equilibrium atomic percentage of Cr through the coating after this initial peak.

Cr target voltage, (V)	Atomic % Cr at the interface
150	~0
200	~0
250	~0.8
300	~1.1
350	~2.3

**Table 4.1 Peak atomic % Cr at the interface with Cr target voltage**

Cr target voltage, (V)	Atomic % Cr
150	0
200	0.5
250	~1
300	~2
350	~8

**Table 4.2 Atomic % Cr in coatings with Cr target voltage**

The profiles obtained for samples prepared at target voltages less than 200V show Cr levels at or below the limit of the calibration of the technique. Above 200V the profiles show a pronounced increase in the level of Cr in the coatings with a maximum concentration at the coating/substrate interface. Taking a specific example, the 300V Cr coating, the level of Cr reaches a maximum of approximately 14 atomic percent at the interface which reduces to a constant level of approximately 2 atomic percent as the coating thickness increases. The atomic percentage of Cr in the coating increases with target voltage.

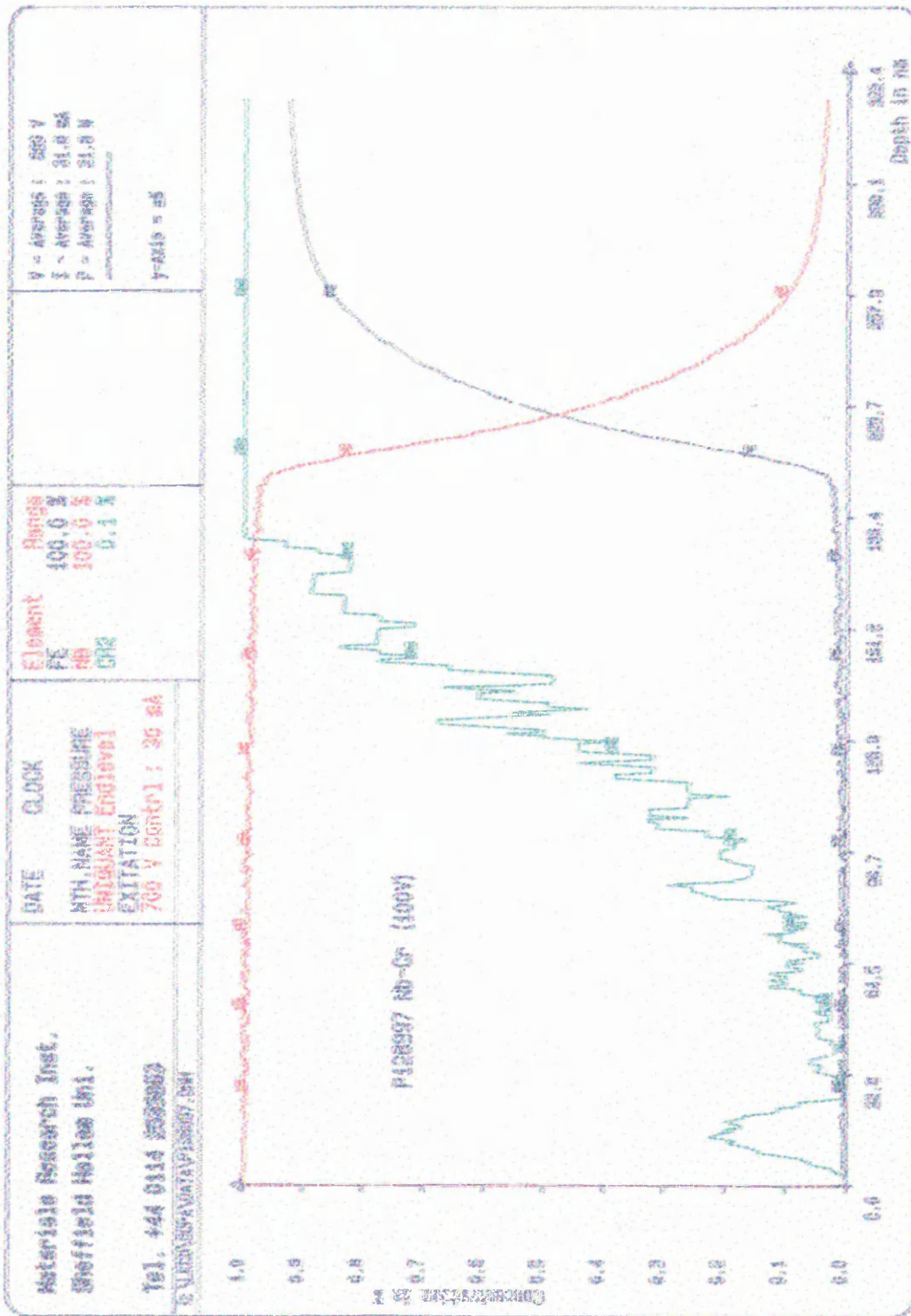


Figure 4.1. GDOES depth profile of Nb-Cr using a Cr target voltage of 100V

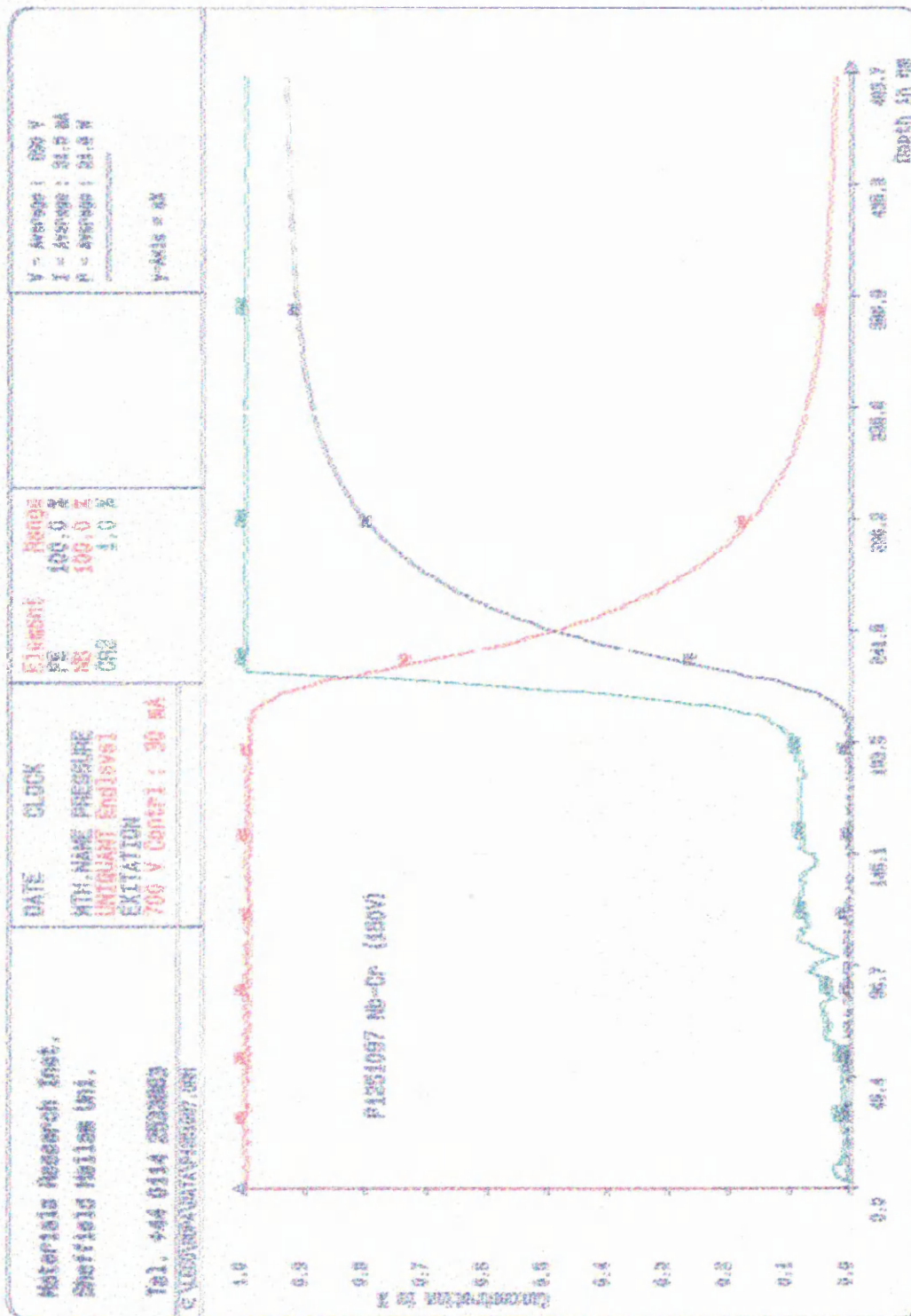


Figure 4.2. GDOES depth profile of Nb-Cr using a Cr target voltage of 150V

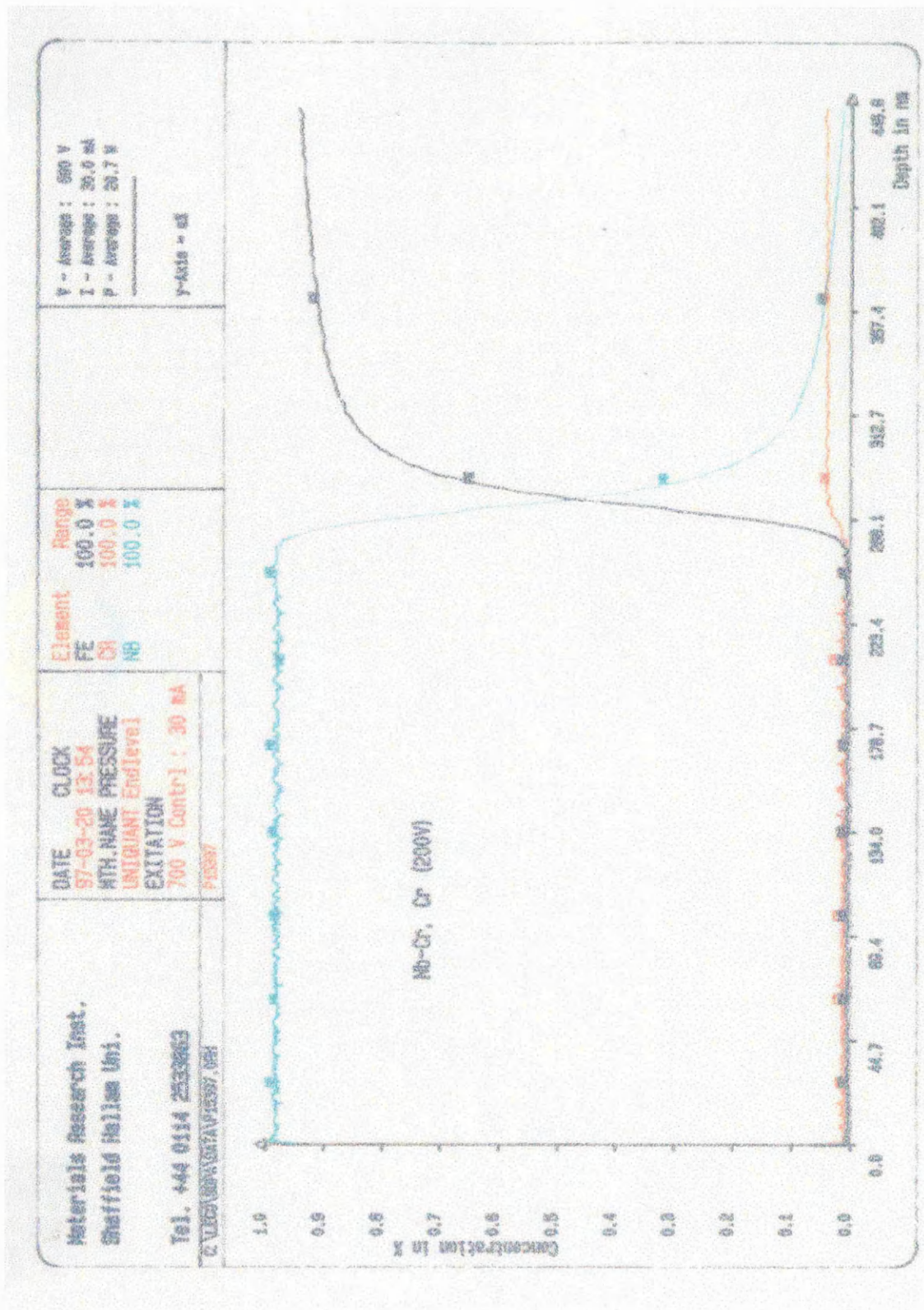


Figure 4.3. GDOES depth profile of Nb-Cr using a Cr target voltage of 200V

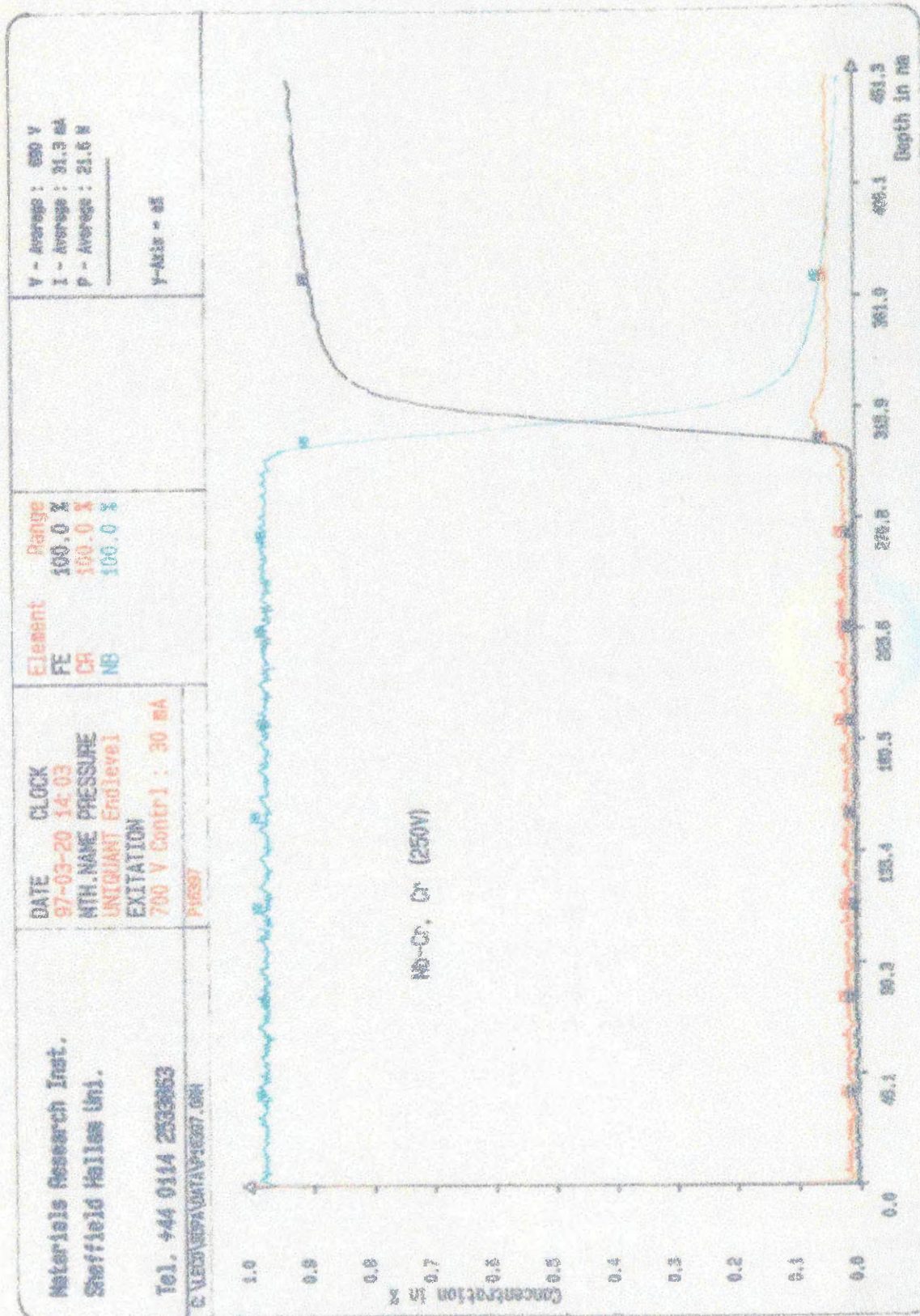


Figure 4.4. GDOES depth profile of Nb-Cr using a Cr target voltage of 250V

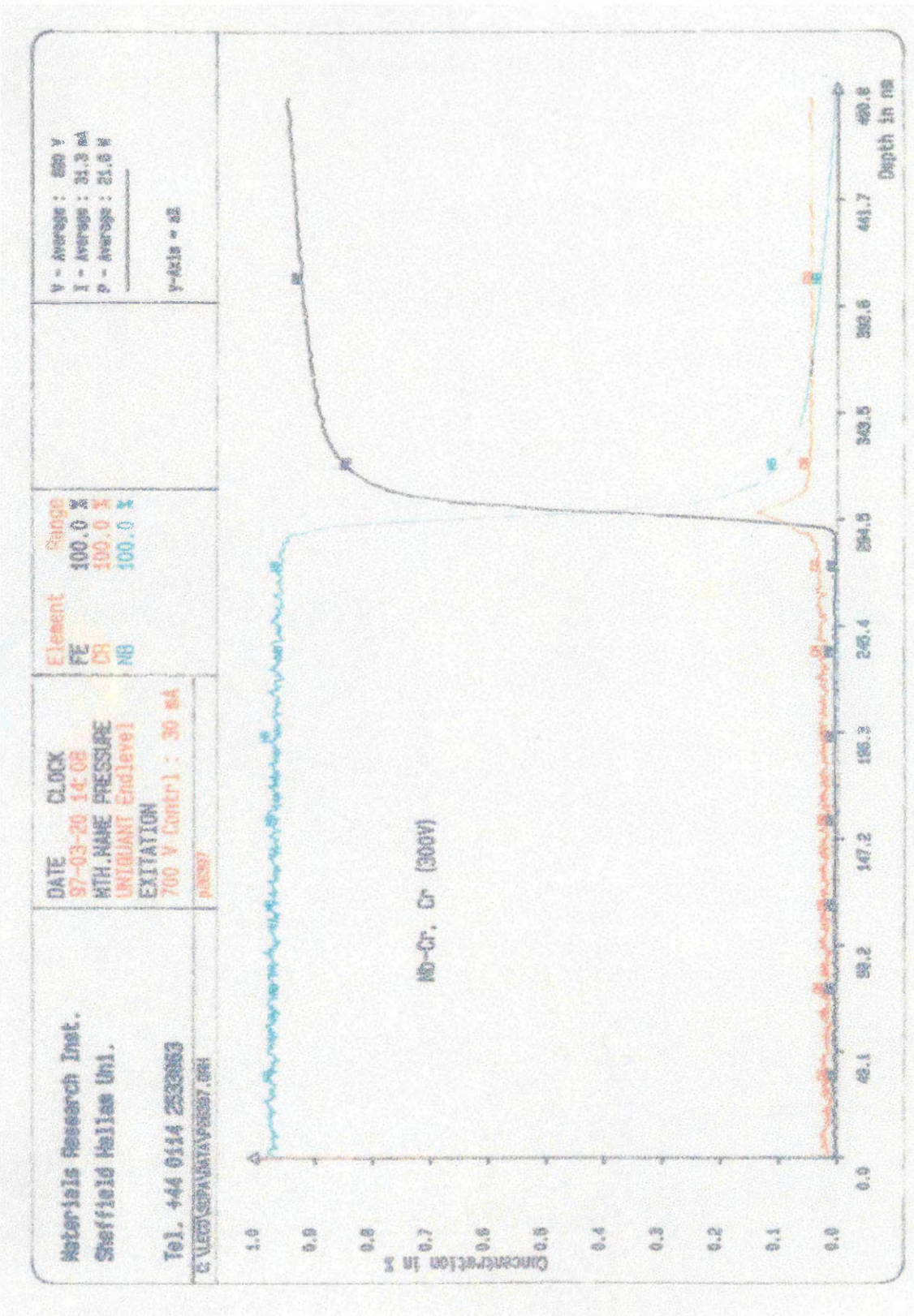


Figure 4.5. GDOES depth profile of Nb-Cr using a Cr target voltage of 300V

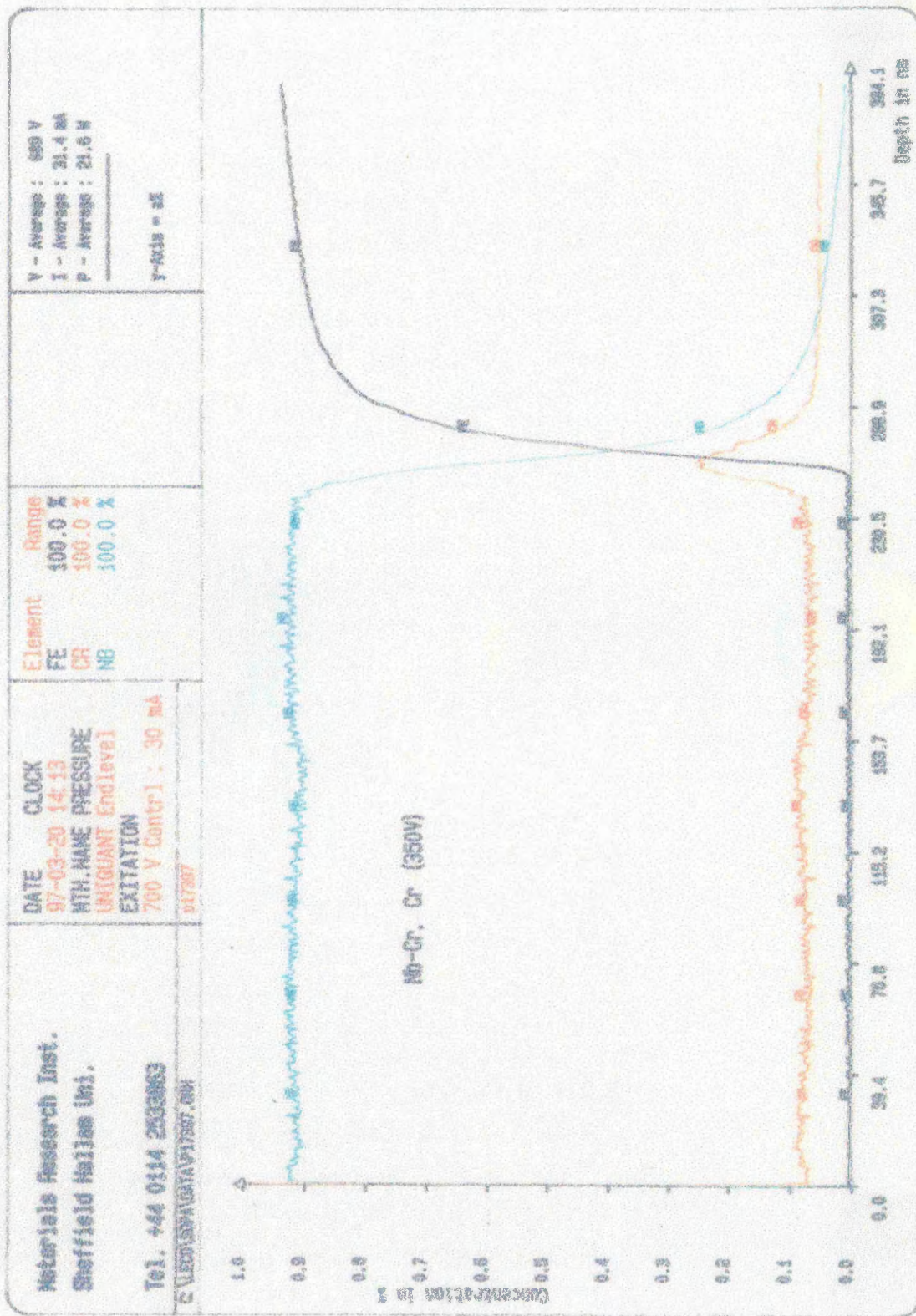


Figure 4.6. GDOES depth profile of Nb-Cr using a Cr target voltage of 350V

## 4.2 X-Ray Diffraction Analysis

### 4.2.1 Diffractometer Traces

The X-ray diffractometer traces of the coatings formed at Cr target voltages of 0, 50, 100, 150, 200, 250, 300, 350V respectively are shown in figures 4.7-4.14. The identification was obtained by comparison with standard powder diffractometry data (100) and the traces are labelled to show these results. The X-ray diffraction analysis shows the crystal structure to be body centered cubic, (b.c.c.) for all the coatings, indicating extensive solid solubility, as would be expected from the phase diagram shown in figure 2.12.

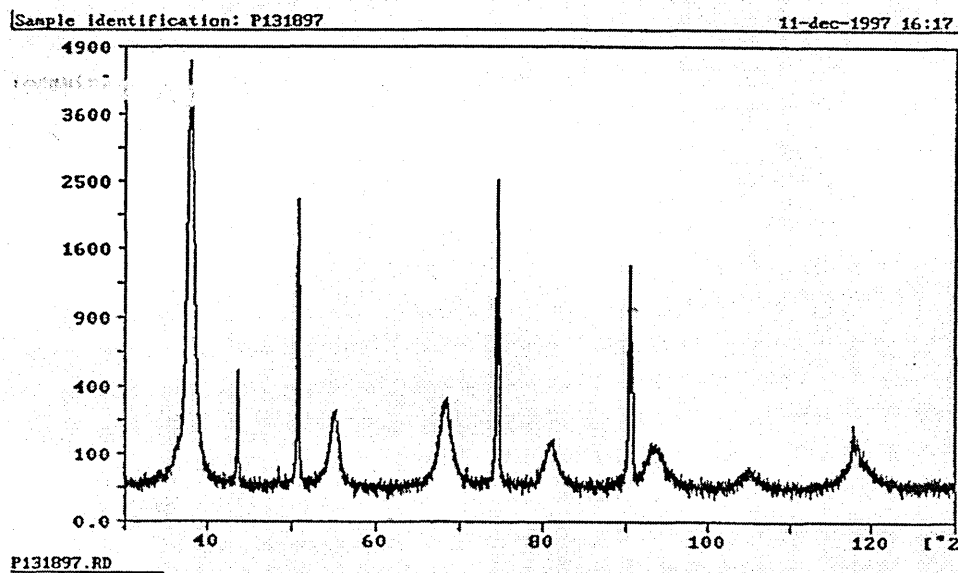


Figure 4.7. X-ray diffraction trace of Pure Nb coating

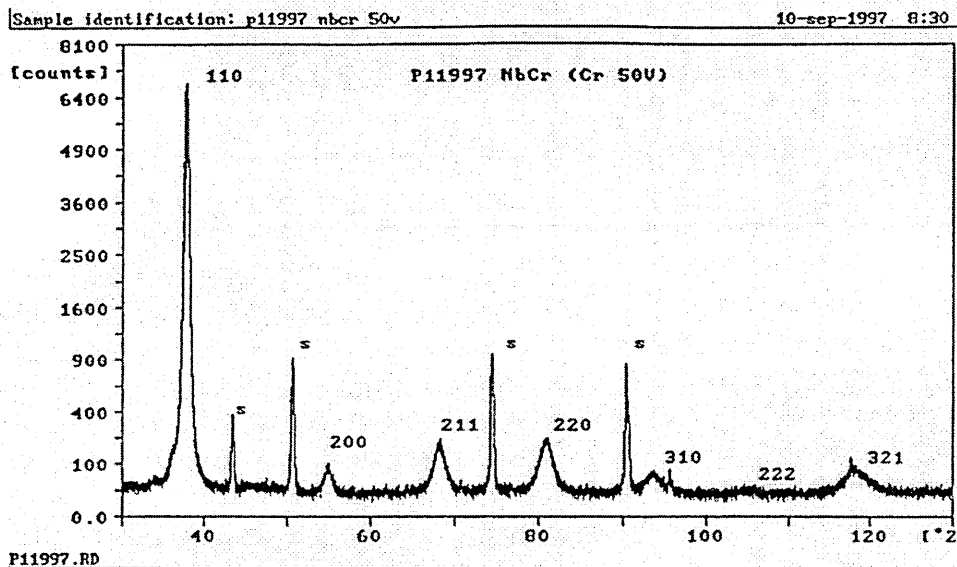


Figure 4.8. X-ray diffraction trace of Nb-Cr (Cr 50V)

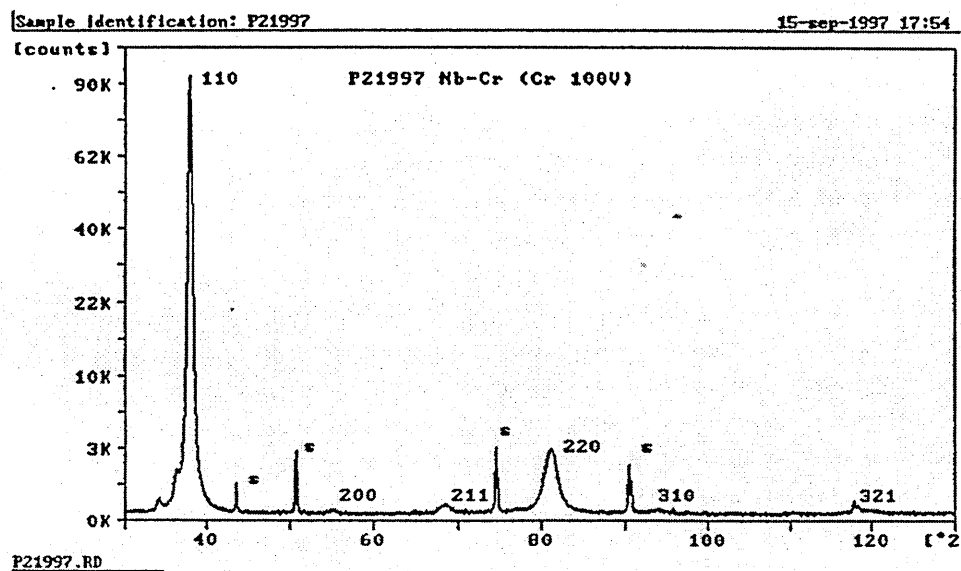


Figure 4.9. X-ray diffraction trace of Nb-Cr (Cr 100V)

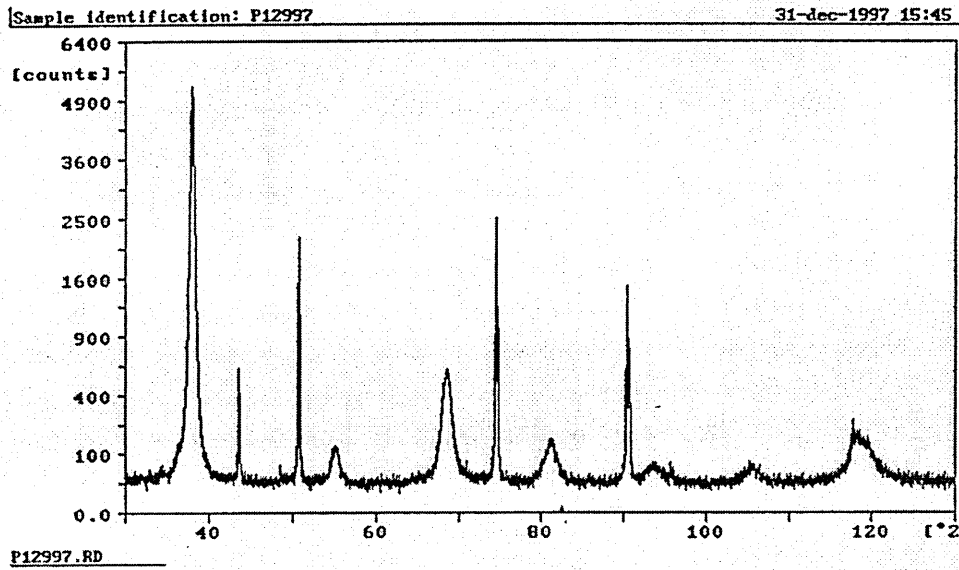


Figure 4.10. X-ray diffraction trace of Nb-Cr (Cr 150V)

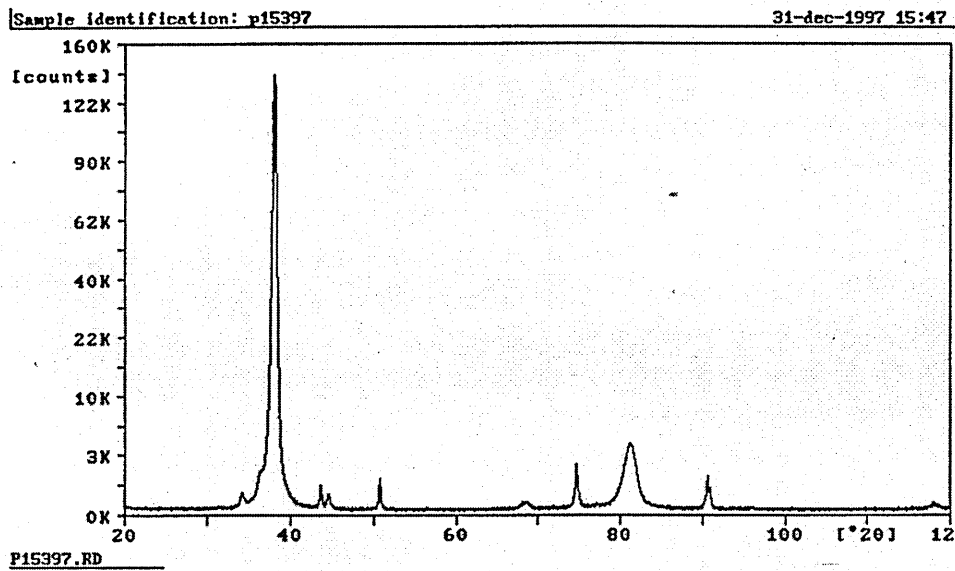


Figure 4.11. X-ray diffraction trace of Nb-Cr (Cr 200V)

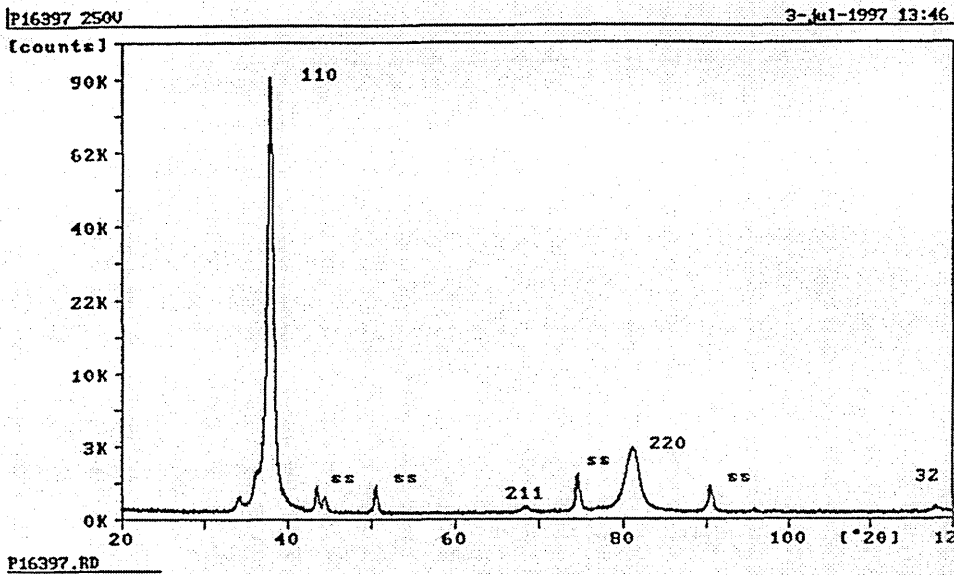


Figure 4.12. X-ray diffraction trace of Nb-Cr (Cr 250V)

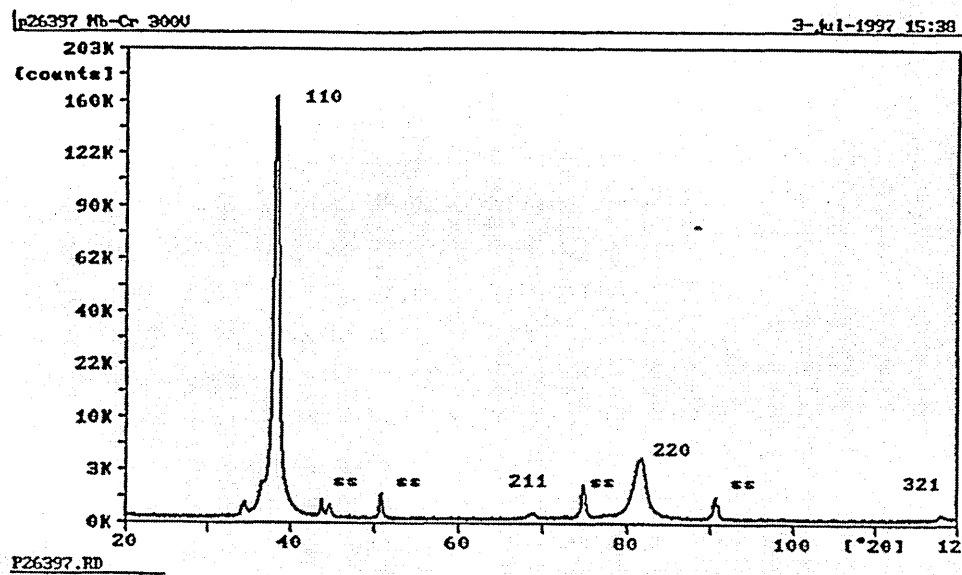


Figure 4.13. X-ray diffraction trace of Nb-Cr (Cr 300V)

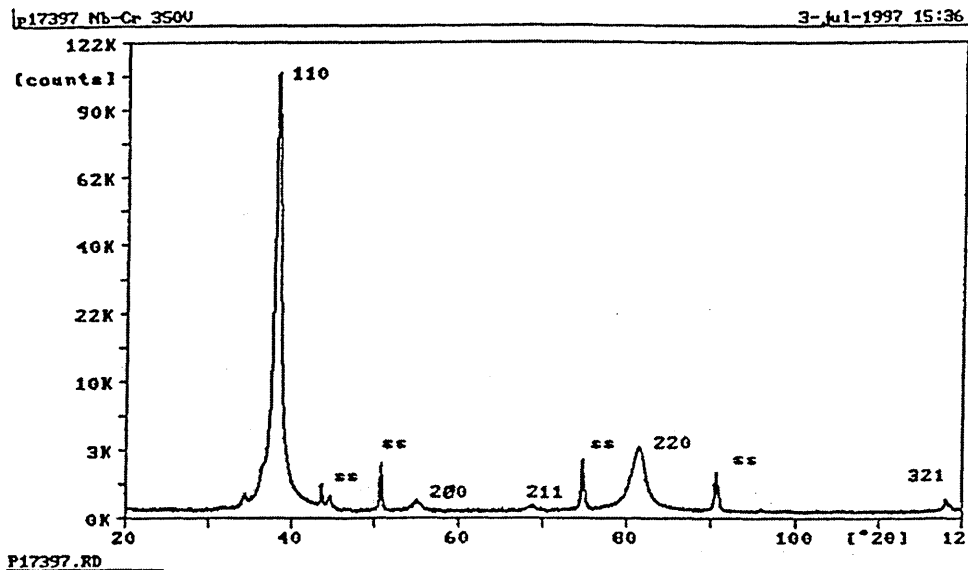


Figure 4.14. X-ray diffraction trace of Nb-Cr (Cr 350V)

#### 4.2.2 Line broadening analysis

Figure 4.15-4.23 show the relationship between  $\beta\cos\theta/\lambda$  and  $\sin\theta/\lambda$  for line broadening observed for Cr target voltages of 0, 50, 100, 150, 200, 250, 300, 350V. The broadening results were obtained for the (110) and (220) reflections in each case. The corresponding intercepts, gradients and associated errors were calculated using Microsoft Excel and are presented in table 4.1 as a function of increasing Cr target voltage.

Repeat peak fitting was carried to determine any error in the analysis, however the same values were given for each measurement. The tabulated errors were therefore calculated by estimating the uncertainty in the measurement of the peak widths and then inserting the maximum and minimum values into  $\beta\cos\theta/\lambda$  and  $\sin\theta/\lambda$ .

Cr target voltage, V	Gradient related to peak broadening to lattice strain	Intercept related to peak broadening due to grain size
0	$0.003 \pm 1.4E-04$	$4E-05 \pm 9.6E-06$
50	$0.0028 \pm 1.2E-04$	$9E-05 \pm 8.3E-06$
100	$0.0024 \pm 1.5E-04$	$2E-05 \pm 9.2E-06$
150	$0.0029 \pm 1.3E-04$	$4E-05 \pm 1.1E-05$
200	$0.0024 \pm 9.0E-05$	$1E-05 \pm 9.8E-6$
250	$0.0024 \pm 1.2E-04$	$4E-05 \pm 9.6E-6$
300	$0.0022 \pm 1.5E-04$	$1E-05 \pm 9.9E-6$
350	$0.0027 \pm 1.4E-04$	$4E-05 \pm 9.8E-06$

**Table 4.1. Gradient and intercept values of  $\beta\cos\theta/\lambda$  vs.  $\sin\theta/\lambda$  with increasing Cr target voltage for Nb-Cr**

The tabulated results show a definite downward influence on the strain values initially as the Cr target voltage was increased from 0V within the estimated experimental error. A maximum is observed at 150V and a minimum at 300V which are at the limit of the estimated errors. The intercepts were very low and in some cases negative.

#### 4.2.3. Asymmetric Bragg-Brentano Stress Analysis

The intrinsic stress in the coatings were calculated from plots of lattice spacing versus  $\sin^2\phi$  using Microsoft Excel as described in section 3.3.1 using equation 3.2. The tabulated errors were calculated from the errors in the gradients. It was intended to determine the Young's moduli and Poisson's ratio for all the alloys using the Fischerscope H100 universal hardness tester, however the coatings proved to be too thin and the determination adversely affected by vibration, for accurate measurement.

Therefore the elastic constants for bulk Nb rather than those of the individual alloys were used. The calculated stress in the coatings is shown for increasing Cr target voltage in table 4.2. As before repeat peak fitting was carried out using the Philips PC-APD software to determine any measurement errors, none were found. The tabulated errors were therefore calculated by estimating the uncertainty in the measurement of the peak positions and then inserting the maximum and minimum values into equation 3.2.

Cr target voltage, (V)	Stress, (MPa)
0	-667±43
50	-918±37
100	-853±48
150	-772±43
200	-884±39
250	-912±31
300	-842±36
350	-911±41

**Table 4.2: Intrinsic stress with increasing Cr, target voltages for Nb-Cr**

Taking into account the use of bulk Nb constants as opposed to measured values, the intrinsic stress increases initially with Cr content, but then reduces to a minimum at a Cr target voltage of 150V. A second minimum is also observed for a target voltage of 300V. Subsequent increases in target voltage after this increases the intrinsic stress in the coating. To determine whether the pronounced reduction in the intrinsic stress of the coating at a Cr target voltage of 150V is a real effect coatings were produced using Cr target voltages between 50 and 200V in increments of 25V. The calculated values of intrinsic stress with Cr target voltage are listed in table 4.3.

Cr target voltage, V	Stress, (MPa)
50	-748±23
75	-788±26
100	-699±21
125	-695±28
150	-631±22
175	-792±23
200	-889±24

**Table 4.3. Intrinsic stress with Cr target voltage in the range 50-200V**

As can be seen the intrinsic stress reaches a minimum at a Cr target voltage of 150V within the estimated experimental error.

#### **4.2.4 Glancing Angle X-Ray Diffraction, (GXR)**

From GDOES analysis, figures 4.1-4.6, it can be seen that Cr targets sputter more efficiently at the early stages of coating, which increases the weight percentage of Cr-contaminant at the interface. It was therefore decided to use glancing angle X-Ray Diffraction to determine the presence of a stress gradient in the coatings using standard values for the Young's modulus and Poisson's ratio of bulk Niobium elastic constants again. The full results are listed in table 4.4. Repeat peak fitting measurements using the X-Ray Diffraction software indicated no error in the peak fitting process. The tabulated errors were calculated by estimating the uncertainty in the measurement of the peak positions and then inserting the maximum and minimum values into equation 3.2.

Cr target voltage, (V)	Stress (-MPa)	
	1°	3°
0	475±18	556±23
50	368±15	468±19
100	384±19	409±22
150	378±16	429±24
200	416±22	407±18
250	418±23	473±22
300	393±17	321±15
350	524±19	458±26

**Table 4.4. Intrinsic stress with increasing Cr target voltage for Nb-Cr using GAXRD and two incident angles.**

A similar trend to that obtained from the  $\text{Sin}^2$  method using the (220) Nb reflection is observed for both the incident angles. The observed stress minima occur at 150V and 300V for the 1 degree incident angle and 250V for the 3 degree case (N.B. bulk Niobium elastic constants were used) with the an expected rise in stress near the interface observed for most samples. Further experiments are needed using different incident angles to determine the presence of a stress gradient within the coating.

#### 4.2.5 Crystallographic Texture

The texture parameters calculated using the method described in section 3.3 are summarised in the table 4.5. Repeat peak fitting measurements using the Philips PC-APD X-Ray Diffraction software indicated no error in the peak fitting process. A '0' indicates no peak was observed.

Cr target Voltage (V)	P for various (hkl)					
	(110)	(200)	(211)	(310)	(222)	(321)
0	1.89	0.75	0.94	1.04	0.25	1.12
50	4.26	0.44	0.5	0.54	0	0.26
100	5.91	0.02	0.03	0.04	0	0
150	2.88	0.54	1.30	0.22	0.51	0.56
200	5.93	0	0.037	0	0	0.031
250	5.94	0	0.025	0	0	0.035
300	5.95	0	0.021	0	0	0.027
350	5.78	0.14	0.02	0	0	0.062

**Table 4.5. Texture analysis of Nb-Cr with increasing Cr target voltage**

Initial measurements of the texture of the films indicated a pronounced reduction in the (110) texture of the Nb-Cr coatings for a target voltage of 150V. Texture values for coatings deposited with Cr target voltages between 50 and 200V with 25V increments were calculated and are shown in table 4.6.

Cr target voltage (V)	P for various (hkl)					
	(110)	(200)	(211)	(310)	(222)	(321)
50	2.4	0.46	0.73	1.46	0	0.94
75	1.70	0.52	1.31	0.73	0.38	1.38
100	3.08	0.53	0.83	0.57	0	0.98
125	32.81	0.32	1.02	0.62	0	1.22
150	3.89	0.52	0.43	0.74	0.04	0.391
175	5.17	0.02	0.26	0.23	0	0.33
200	2.97	0.37	0.94	0.61	0.03	1.08

**Table 4.6. Repeat texture analysis of Nb-Cr coatings deposited using Cr target potentials in the range 50-200V.**

The pronounced reduction in texture for the coating deposited at 150V was not observed for the repeat measurements

#### 4.2.6 Omega Scan

Due to the highly (110) textured nature of the original set of coatings Omega scans were used to give an indication of the degree of orientation (100). The detector was set at the maximum intensities of the (110) and (220) reflections and then rocked around this point, from 0 to 37 degrees for the (110) reflection and from 0 to 80 degrees for the (220) reflection.. The Full Width at Half Maximum, FWHM of the subsequent diffraction peak indicates the degree of orientation. The peaks were fitted using the Philips software as before. The results are listed in table 4.7.

Cr target voltage (V)	(hkl) Reflection	Position $\omega$ (°)	FWHM (°)
0	(110)	$19.55 \pm 0.05$	$16.87 \pm 0.05$
	(220)	$40.84 \pm 0.05$	$31.75 \pm 0.05$
50	(110)	$18.08 \pm 0.05$	$17.05 \pm 0.05$
	(220)	$40.54 \pm 0.05$	$32.41 \pm 0.05$
100	(110)	$19.05 \pm 0.05$	$9.41 \pm 0.05$
	(220)	$40.64 \pm 0.05$	$7.91 \pm 0.05$
150	(110)	$18.74 \pm 0.05$	$20.72 \pm 0.05$
	(220)	$38.49 \pm 0.05$	$48.70 \pm 0.05$
200	(110)	$18.01 \pm 0.05$	$8.76 \pm 0.05$
	(220)	$39.47 \pm 0.05$	$7.78 \pm 0.05$
250	(110)	$18.47 \pm 0.05$	$6.06 \pm 0.05$
	(220)	$40.02 \pm 0.05$	$6.16 \pm 0.05$
300	(110)	$19.07 \pm 0.05$	$7.52 \pm 0.05$
	(220)	$40.65 \pm 0.05$	$7.10 \pm 0.05$
350	(110)	$19.09 \pm 0.05$	$8.70 \pm 0.05$
	(220)	$40.67 \pm 0.05$	$8.62 \pm 0.05$

**Table 4.7. Omega (Rocking) Scans for the (110) and (220) Nb reflections for Nb-Cr alloys**

As can be seen again the least textured sample is the 150V case indicated by the broadest rocking curve. As the repeat set of coatings in the 50-200V range were not as textured as the original set of coatings omega scans were not carried out.

### 4.3 Universal Hardness

The nanoindentation measurements for the samples with Cr target voltages in the 0V-350V range showed no clear trend in the depth of penetration with Cr target voltage for a constant load. Elastic moduli can theoretically be calculated from the gradient of the unloading curve (101). However, in most of the cases an error of over 50% was observed, indicating that the thickness of the coatings needs to be greater to give an accurate measurement of the hardness and elastic moduli.

### 4.4 Rockwell adhesion

The Rockwell tests consistently showed no signs of spallation around the circular indent, figure 4.17 shows an SEM image of one of the indents.

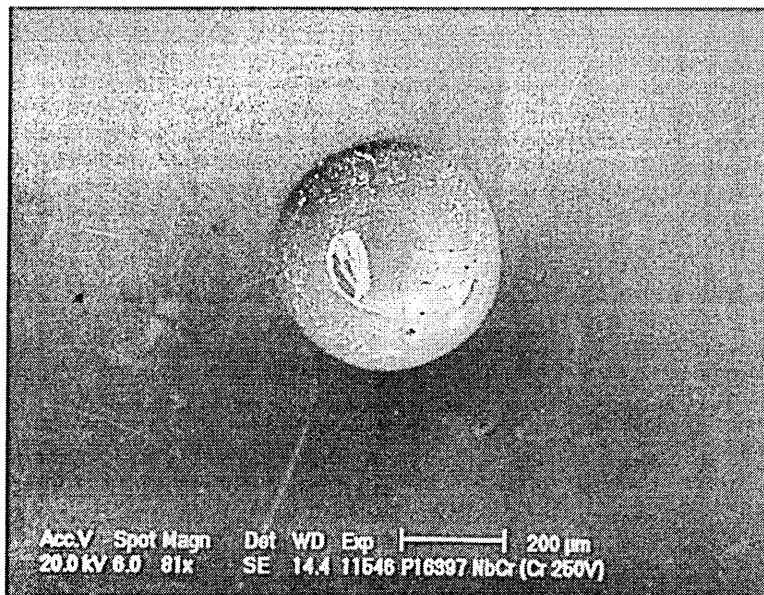


**Figure 4.17. SEM image of a Rockwell indent**

#### 4.5 Corrosion test

Figures 4.18a and 4.18b show the anodic polarization curves for co-sputtered Nb-Cr alloy films and an M2 HSS sample in a 3% NaCl solution

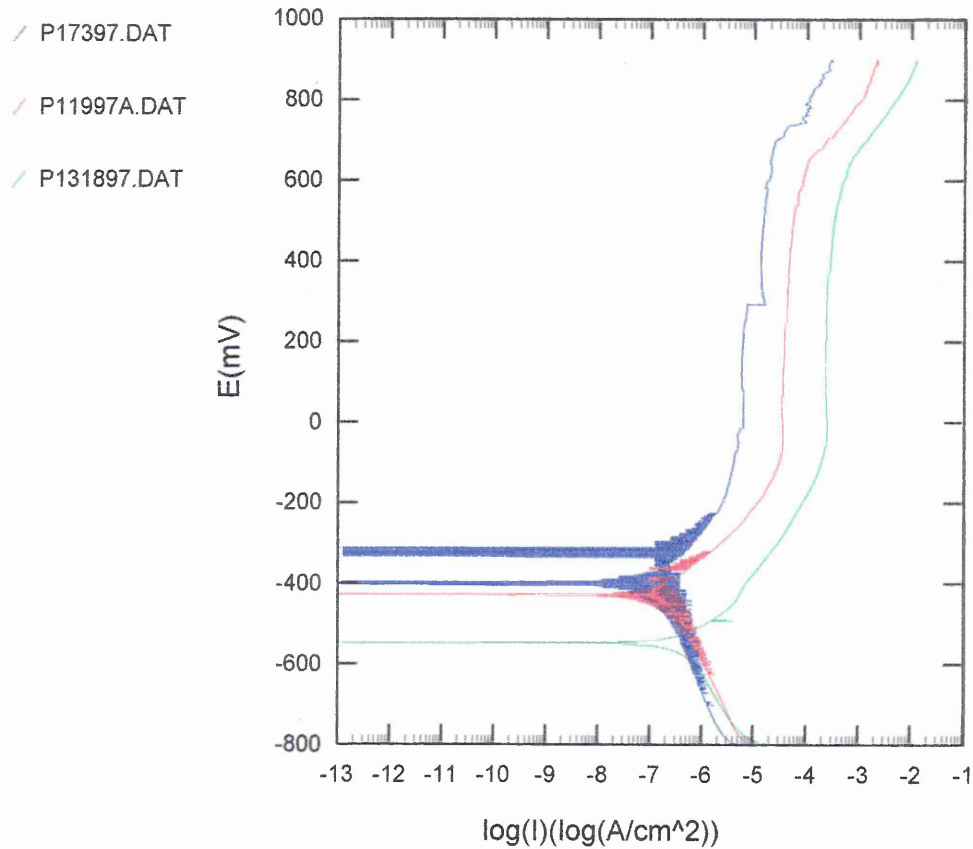


**Figure 4.18a. Potentiodynamic polarization curves for a pure Nb (P131897), Nb-Cr (Cr 50V) (P11997), Nb-Cr (Cr 350V) (P17397). Tested in 3% NaCl solution at room temperature**

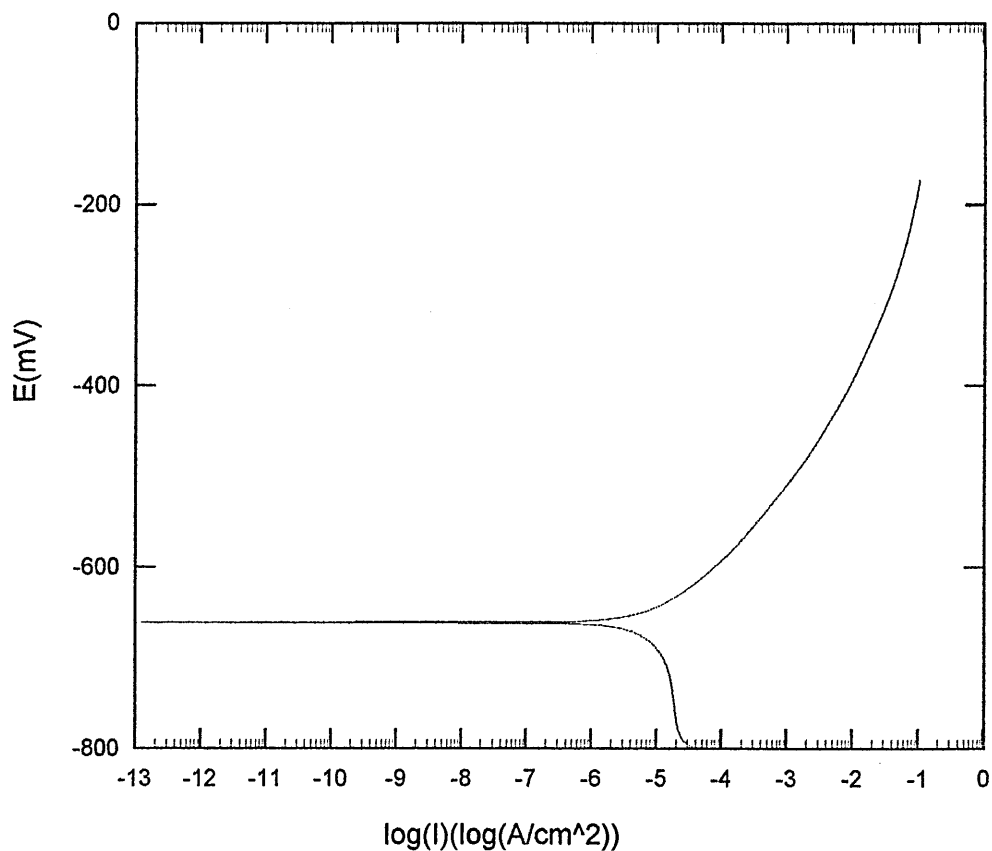


**Figure 4.18b Potentiodynamic polarization curve for uncoated M2 High Speed Steel**

The corrosion behaviour of the tested samples is shown in figure 4.18. It can be seen that passivation, due to the formation of a thin  $\text{Nb}_2\text{O}_5$  surface layer, occurs over a similar potential range for all the samples, ( $\sim 0\text{mV}$ - $630\text{mV}$ ). The pitting potential, the point at which the oxide layer begins to break down is similar for all coatings ( $\sim 630\text{V}$ ). All the current densities are higher than that of bulk Nb.

The maximum corrosion resistance of the coatings was observed for the film with the highest atomic % Cr ( $\sim 8\%$  according to GDOES), P17397. It was also found that although a target voltage of  $50\text{V}$  is insufficient to result in sputtering, the corrosion resistance of the sample deposited with the Cr target set at  $50\text{V}$  (P11997) was higher than that of the “pure” Nb coating, (P131897). All samples performed better than the uncoated M2 HSS substrate. Figures 4.19-4.22 show SEM images of the corroded areas of the samples tested, pitting can be clearly seen.

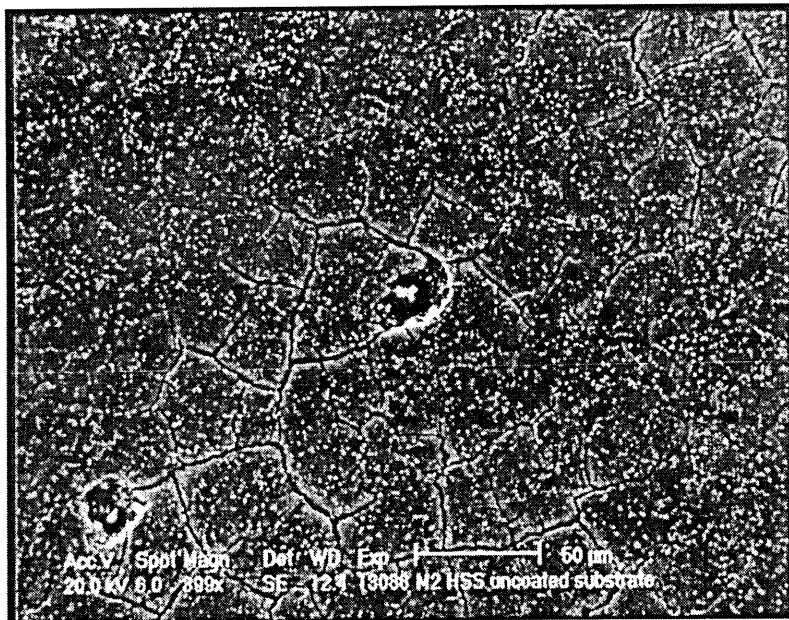


**Figure 4.19 SEM image of the corroded area of the uncoated M2 HSS substrate**



**Figure 4.20. SEM image of “pure” niobium coating**

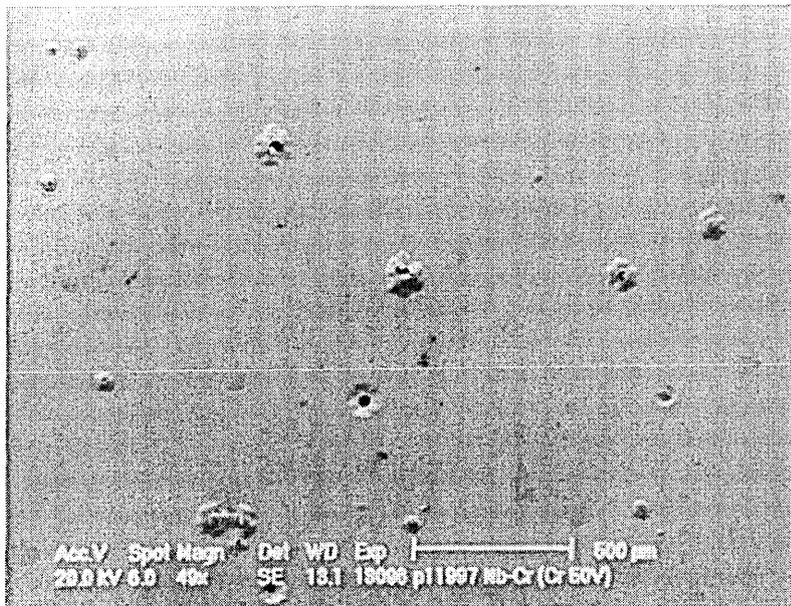


Figure 4.21. SEM image of the Nb-Cr (50V) coating



Figure 4.22. SEM image of the Nb-Cr (350V) coating

## 4.6 Friction Tests

Figures 4.23-4.29 show friction coefficient  $\mu$  vs. the sliding distance for a number of Nb-Cr samples with increasing Cr target voltage, (all of the samples could not be tested due to a lack of sample area after other characterisation tests) using a CSEM tribometer pin-on-disc wear and friction system. A constant normal load of 1N and a sliding speed of  $1 \times 10^{-2} \text{ ms}^{-1}$  were used. The measured coefficient of friction for all samples are listed in table 4.7.

Cr target voltage, V	Initial measured value of the coefficient of friction, $\mu_i$	Final measured value of the coefficient of friction, $\mu_f$
0	0.7	0.2
50	0.42	0.27
75	0.93	0.3
100	0.33	0.33
125	0.68	0.33
175	1.15	0.45
250	1.19	0.52

**Table 4.8 Table showing the initial and final values of the coefficient of friction of Nb-Cr coatings deposited with different Cr target voltages.**

For most of the samples  $\mu$  increases rapidly initially, with Nb-Cr (Cr 100V) the exception. From these initial results it may be said that qualitatively the coefficient of friction of the coating increases with Cr target voltage. However, further testing is needed using further samples and different sampling rates before this conclusion can be confirmed.

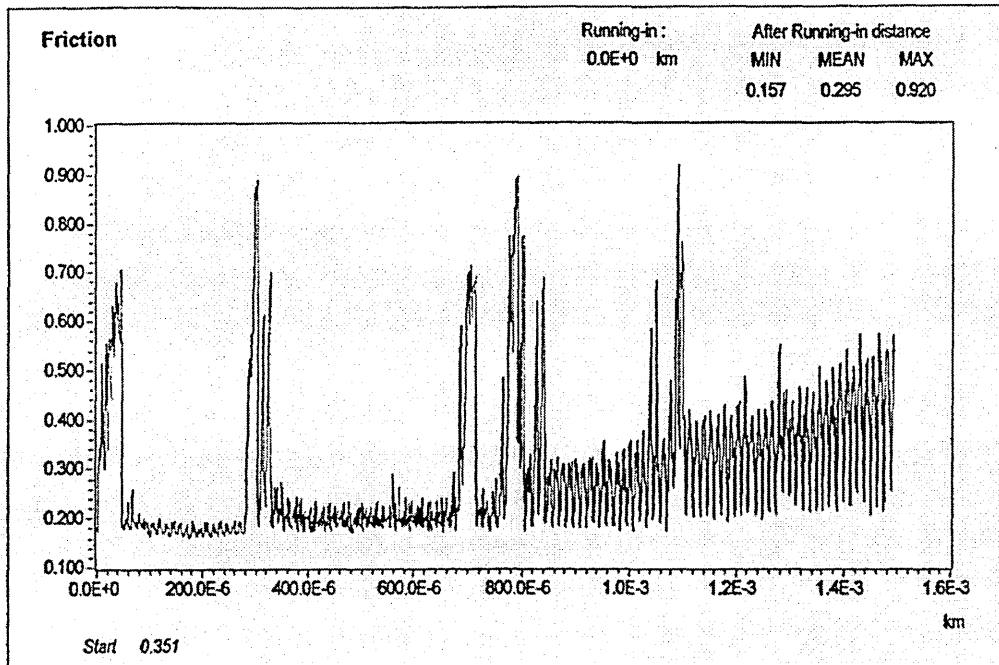


Figure 4.23 Friction coefficient evolution vs. Sliding distance for “pure Nb” coating

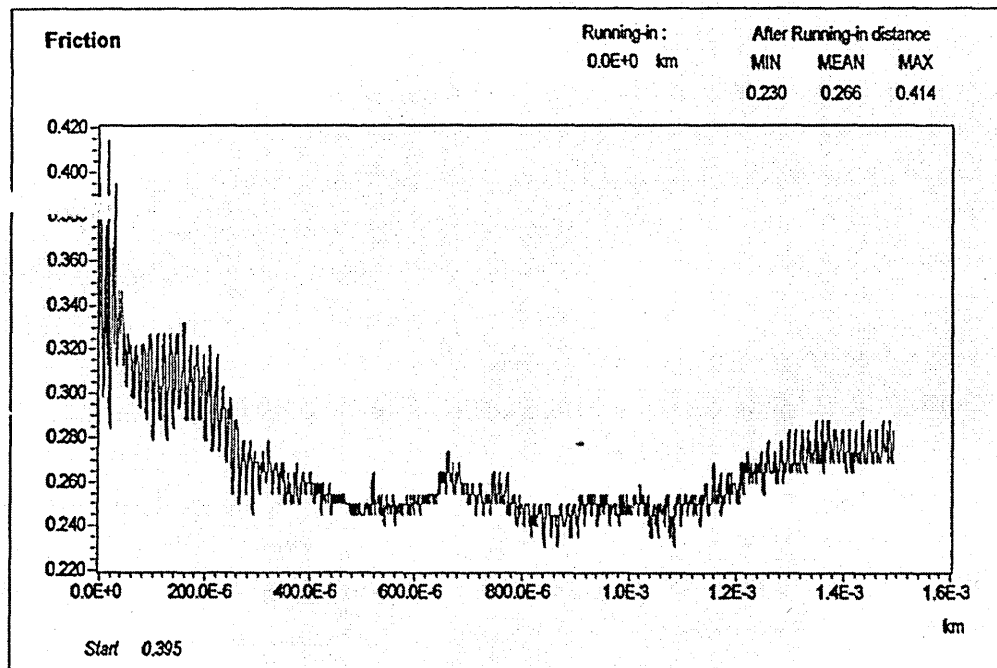


Figure 4.24 Friction coefficient evolution vs. Sliding distance for Nb-Cr (Cr 50V) coating

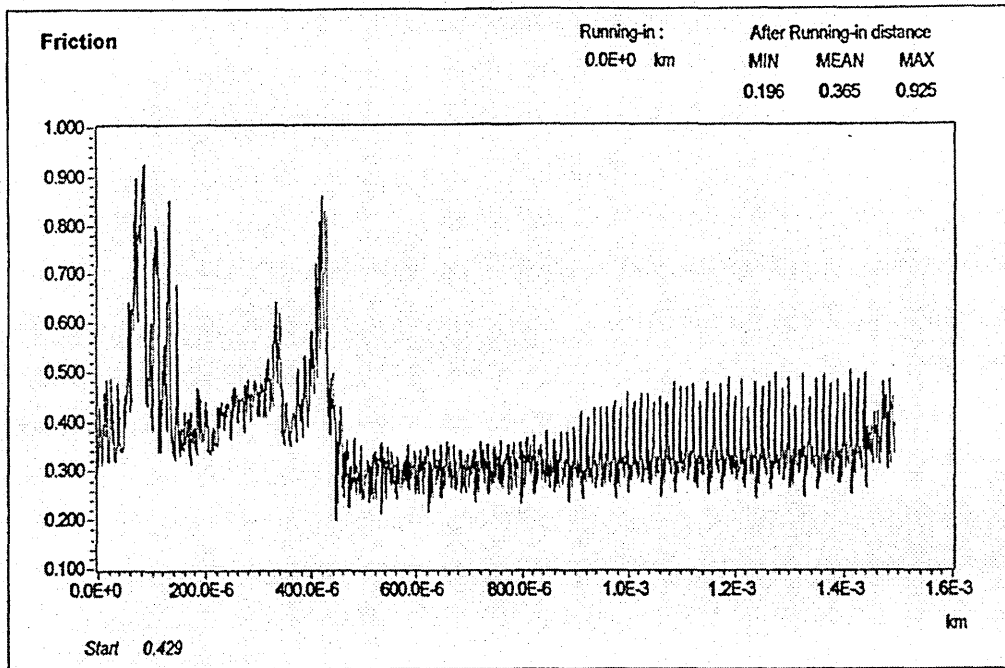


Figure 4.25 Friction coefficient evolution vs. Sliding distance for Nb-Cr (Cr 75V) coating

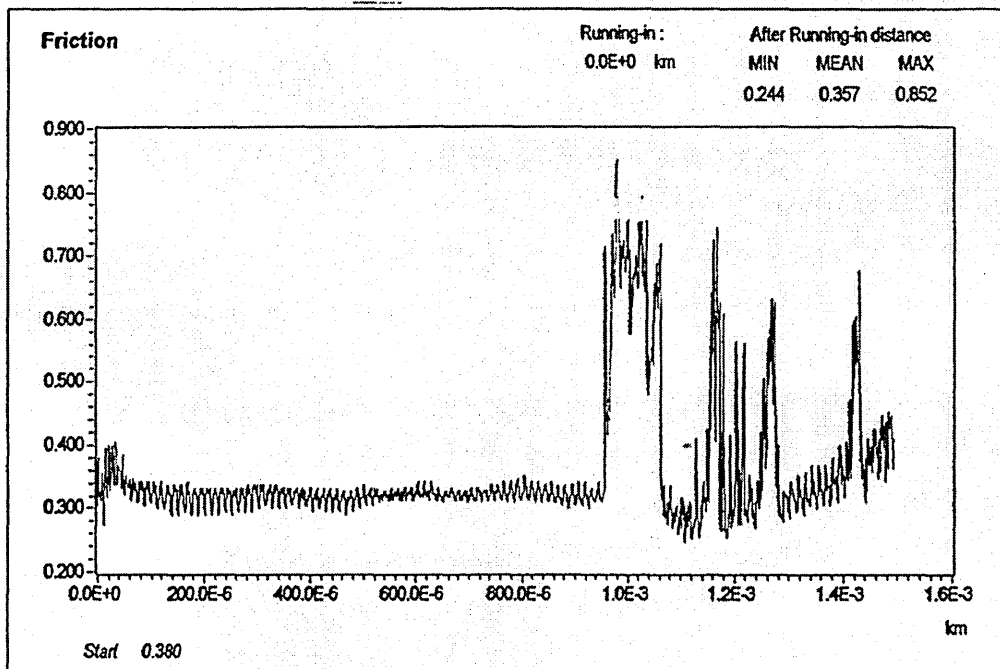
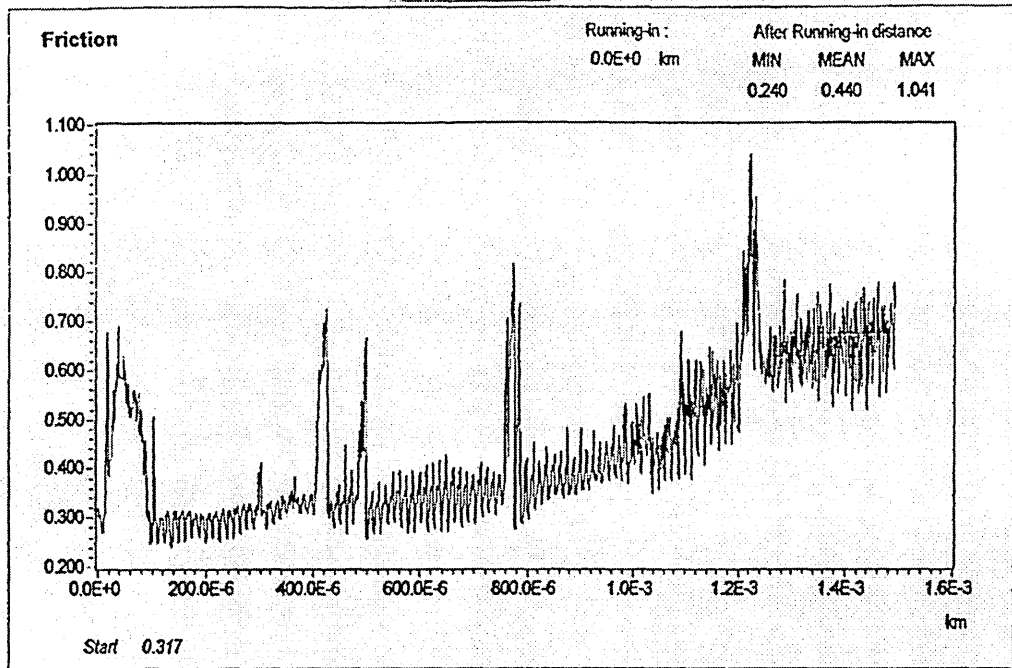
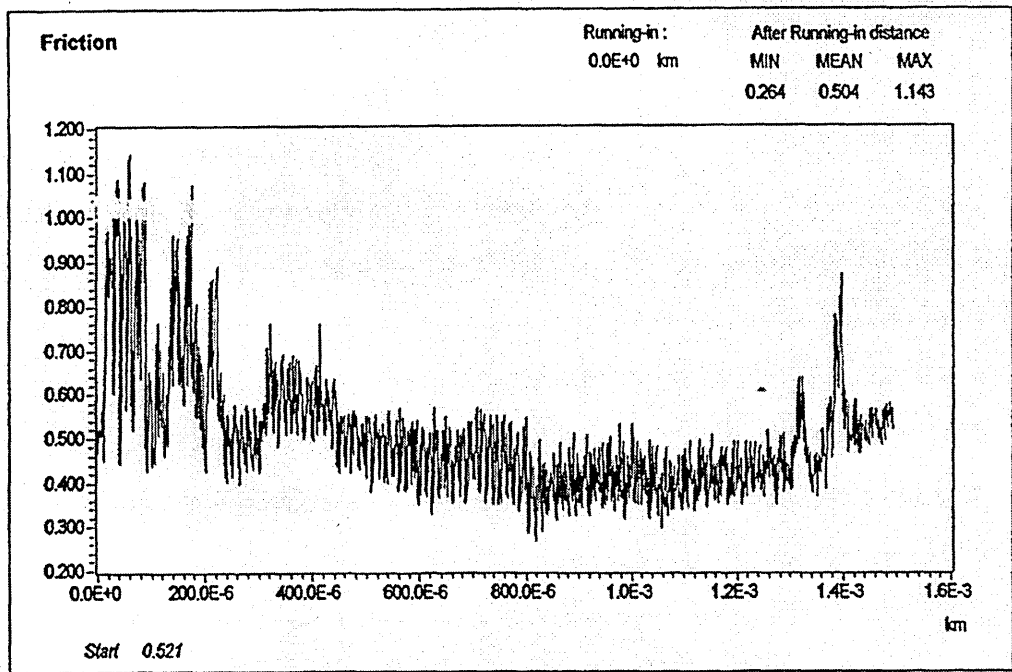


Figure 4.26 Friction coefficient evolution vs. Sliding distance for Nb-Cr (Cr 100V) coating



**Figure 4.27 Friction coefficient evolution vs. Sliding distance for Nb-Cr (Cr 125V) coating**



**Figure 4.28 Friction coefficient evolution vs. Sliding distance for Nb-Cr (Cr 175V) coating**

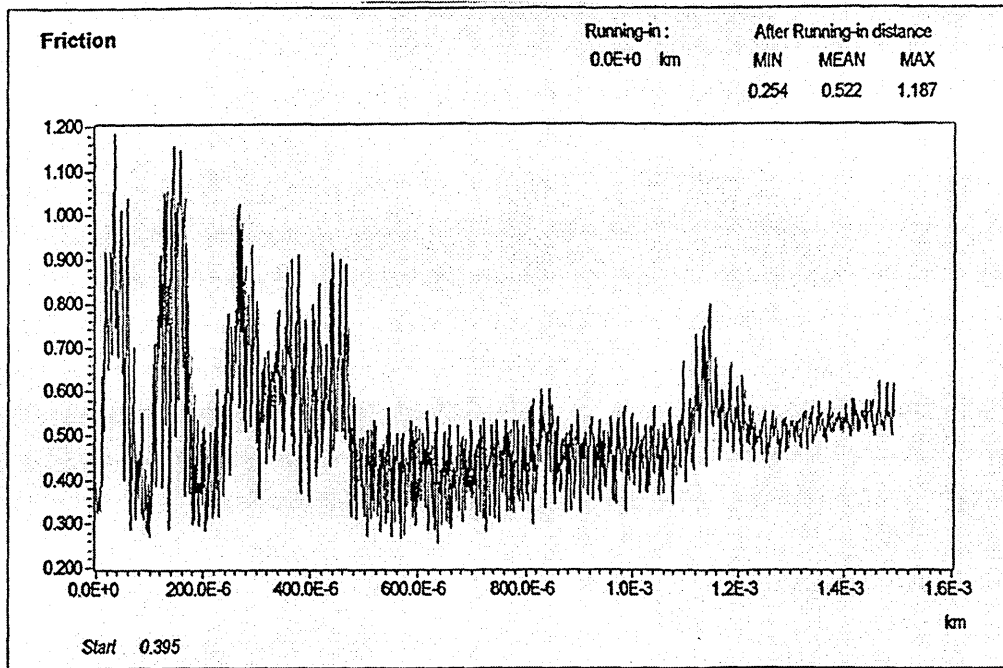


**Figure 4.29 Friction coefficient evolution vs. Sliding distance for Nb-Cr (Cr 250V) coating**

## 5. Discussion

The aim of this investigation was to determine the effect of Cr target voltage on the sputter deposited Nb coatings. This was investigated by manufacturing a series of coatings in the Hauzer HTC 1000-4 ABS<sup>TM</sup> system using the same set-up and process parameters except for varying the Cr target voltage from 0V to 350V in steps of 25/50 volts. The chemical composition of the coatings was determined using GDOES, which indicated levels of Cr in the coatings at the limit of calibration of the technique for target potentials below 200V. For samples coated at potentials above 200V it revealed an increase in Cr deposition at the coating/substrate interface for all samples, which increased in concentration with target voltage. This was seen as due to the clean target's higher sputter yield at higher target voltages.

After this initial peak, the level of Cr in the coatings decreased with increasing coating thickness until a dynamic equilibrium was established between sputtering Cr and deposition of Nb onto the Cr target. This resulting equilibrium level of Cr in the coatings increased with Cr target voltage due to the increased energy of the incoming ions resulting in a higher sputter yield.

The structure of the coatings was determined using X-ray diffractometry, (XRD) and showed all coatings to have a body centered cubic (BCC) lattice with extensive solid solubility as one would expect from the phase diagram, (figure 2.12). XRD also gave an indication of the texture of the coatings (table 4.4) which were predominantly (110) which is the most densely packed plane and therefore the most energetically favourable orientation. A pronounced reduction in texture was noted for the sample deposited with a Cr target voltage of 150V, however further coatings deposited using Cr target voltages between 75V and 200V failed to repeat this behaviour. XRD line broadening analysis indicated very large grained structures for all samples (0V, 50V, 100V, 150, 200, 250, 300, 350V). To give an indication of the error in the XRD measurements (texture, line broadening, stress, omega scans)

repeat peak fitting was carried out. The results showed no deviation in the fitting process.

Analysis using asymmetric Bragg-Brentano geometry carried out at Sheffield Hallam University, and GAXRD at Hull University, (tables 4.2-4.4) showed a reproducible form of stress behaviour with increasing Cr target voltage. While absolute values varied as would be expected, a pronounced minimum was observed in both sets of data for a target voltage of 150V, which was also observed for repeat coatings using the asymmetric Bragg-Brentano method (table 4.3). Table 4.4 shows that GAXRD revealed an increase in the level of stress at the substrate/coating interface for most samples. This increase in the level of stress at the interface can be explained by the higher atomic % of Cr at the interface as revealed by the GDOES depth profiles, (figures 4.1-4.6).

Rockwell indentation tests showed no spallation around the circular indent for all coatings indicating good adhesion.

Ultramicrohardness measurements showed no general trend in the hardness of the coatings with increasing Cr content over the measured range. However, this may be due to the thickness of the coatings (~0.4 $\mu$ m) which are of a magnitude where the effect of the substrate can not be ignored.

Friction tests indicated an increase in the average coefficient of friction with Cr target voltage, although further work is needed to determine the reproducibility of this result.

Corrosion tests, the results of which are shown in figure 4.18 showed the coating deposited with a Cr target voltage of 350V was the most resistant to alkaline attack, followed by the coating deposited with a Cr target voltage of 50V, and finally the "pure Nb" coating. This can be seen clearly from the SEM micrographs of the

topography of the surfaces of the coatings, shown in figures 4.19-4.22. All coatings performed better than the HSS substrate.

GDOES has shown the presence of a greater Cr atomic % at the interface for target voltages greater than 200V, which corresponds to an increase in stress as shown by GXRD. Corrosion tests indicated improved coating resistance to alkaline attack with increasing Cr target voltage, which agreed with work published by J.H. Hsieh and co-workers (102). They found that concurrent bombardment during deposition with low energy ions (100-1000eV) improved the structure and density of the Nb coatings due to increased adatom mobility. An alternative method to improve the coating structure and density of niobium, that they used, was to co-deposit with chromium. Further improvement was found using a combination of both ion bombardment and codeposition, (by increasing the Cr target voltage we have increased the level of ion bombardment and the atomic % of Cr in the coating). The results also agreed with other published work by Brooker (103) and Mawella and Sheward (104) who found that simultaneously depositing two metals that have different atomic radii (e.g. Nb and Cr) reduces self-shadowing effects, producing denser microstructures.

## 6. Further Work

A series of further experiments is needed using longer deposition times as thicker coatings are required for mechanical testing, especially for the accurate determination of ultramicrohardness. This would also enable the elastic constants for the coatings to be evaluated for stress measurements. Care must be taken however, to ensure the setup of the vacuum chamber remains constant throughout so the existence of a possible relationship between stress and texture can be determined. Further friction measurements are needed using different measurement speeds to determine the reproducibility of the results obtained so far. A series of further corrosion measurements is required on samples deposited using a broader range of Cr target voltages to confirm the observed behaviour.

This study has given an indication of the effect of Cr target voltage and therefore Cr cross-contamination on the properties of co-sputter deposited films. The further work recommended should show the effect of the Cr target voltage on the mechanical properties of the coating and lead to an overall understanding of the fundamental processes involved.

7. **References**

1. B.N. Chapman, "*Glow Discharge Processes*", Wiley Interscience Press, 1980
2. E. Ertürk, O. Knotek, W. Burgmer, H.-G. Prengel, H.-J. Heuvel, H.-G. Dederichs, C. Stössel, (1991), *Surf. Coat. Tech*, 46, 1, 39-46.
3. W.-D. Münz, D. Schulze and F.J.M. Hauzer, (1992) *Surface and Coatings Technology*, 50, 169-178.
4. W.-D. Münz, D. Schulze and F.J.M. Hauzer, (1992) *Surface and Coatings Technology*, 50, 169-178.
5. W.R. Grove, (1842), *Phil. Trans. Roy. Soc. London*, 142, 87.
6. E. Goldstein, (1902), *Verh. Disch. Phys. Ges*, 4, 228-237
7. O. Almen, G. Bruce, (1961), *Nucl. Instrum. Methods*, 11, 257-279.
8. R. Behrisch, *Sputtering by Particle Bombardment I*, Springer-Verlag Berlin Heidelberg New York, 1981.
9. R.V. Stuart and G.K. Wehner, (1981) *J. Appl. Phys.* V33, 19812345.
10. L.I. Maissel and R. Glang, '*Handbook of Thin Film Technology*', McGraw-Hill Book Company, 1983.
11. M. Konuma, "*Film Deposition by Plasma Techniques*", Springer-Verlag, 111, 1992.
12. R. Behrisch, "*Sputtering by Particle Bombardment*" I, Springer-Verlag Berlin Heidelberg New York 1981.
13. B.N. Chapman, "*Glow Discharge processes*", Wiley New York Press, 1980.
14. D.S. Rickerby and A. Matthews, '*Advanced Surface Coatings: A Handbook of Surface Engineering*', Blackie & Son Limited, 1991.
15. F. I. Boley, '*Plasma-Laboratory and Cosmic*', D. Van Nostrand Company, INC. 1966.
16. R.W. Berry, P.M. Hall, and M.T. Harris, '*Thin Film Technology*', Van Nostrand Reinhold Company New York, 1968.
17. L.I. Maissel and R. Glang, '*Handbook of Thin Film Technology*', McGraw-Hill Book Company, 1983.
18. B. Bhushan and B.K. Gupta, *Handbook of Tribology, Materials, Coating, and Surface Treatments*, McGRAW-HILL, INC. (1991) 959.

19. R.P.Howson, H.A.J' afer, A.G. Spencer, (1990), *Thin Solid Films*, 193/194,127.
20. G.N. Jackson, (1970), *Thin Solid Films*, 5, 209.
21. R.F. Bunshah, J.M. Blocher, and coworkers, "*Deposition Technologies for Films and Coatings*", 1982.
22. B.N. Chapman, "*Glow Discharge processes*", Wiley New York Press, 1980.
23. D.S. Rickerby and A. Matthews, "*Advanced Surface Coatings: A Handbook of Surface Engineering*", Blackie & Son Limited 1991.
24. F.M. Penning, (1936), *Physica*, V3873.
25. R.K. Waits, (1978), *Journal of Vacuum Science Technology*, V15, 179.
26. S. Swann, (1987), *Journal of Vacuum Science Technology*, A5 1750.
27. J. Cuomo and S.M. Rosnagel, (1986), *Journal of Vacuum Science Technology*, A4, 393.
28. P.S. Mcleod and L.D. Hartsough, (1977), *Journal of Vacuum Science Technology*, V14, 263.
29. R.K. Waits, (1978), *Journal of Vacuum Science Technology*, V15179.
30. J.A. Thornton and A.S. Penfold, (1978), *Journal of Vacuum Science Technology*, V15, 171.
31. J.A. Thornton, SAE report ~730544, 1973, SAe, New York, USA.
32. J.A. Thornton, A.S. Penfold, "*Thin Film Processes*", Academic New York Press, 1978.
33. J.A. Thornton, (1974) *J.Vac.Sci.Technol*, 11(4). 666-670.
34. J. Almeida, (1989) *Vacuum*, V39717.
35. S. Kadlec, J. Musil, W.-D. Münz, G. Hakanson, and J.-E. Sundgren, (1989) *Surface & Coating Technology*, V39/40 487-497.
36. I. Petrov, L. Hultman, U. Helmersson, J-E. Sundgren, and J.E. Green, (1989), *Thin Solid Films*, V169 299.
37. D.S. Rickerby and A. Matthews, *Advanced Surface Coatings: A Handbook of Surface Engineering*, Blackie & Son Limited, 1991.
38. J. Viskocil, J. Musil, S. Kadlec, W-D. Münz, *Plasma.Surf.Eng.*88, 1989, Garnisch-Partenkirchen, DGM Informationsgesellschaft Verlag, 665.
39. W. Yao, S. Tung, W. Shi, Z. Qi, (1989), *Plasma. Surf. Eng.*, 1, 633.
40. B. Window and N. Savvides, (1986) *Journal of Vacuum Science and*

- Technology*, A4, 6
41. B. Window and N. Savvides, (1986) *Journal of Vacuum Science and Technology*, A4, 453.
  42. N. Savvides and B. Window, (1986), *Journal of Vacuum Science and Technology*, A4, 504.
  43. R. Nyaeish, (1981), *Thin Solid Films*, 86 267-277.
  44. B. Window and G.L. Harding, (1990), *Journal of Vacuum Science and Technology*, A8, 1277.
  45. S.L. Rohde, I. Petrov, W.D. Sproul, S.A. Barnett, P.J. Rudnik and M.E. Graham, (1990), *Thin Solid Films*, V193/194 117.
  46. S. Schiller, E. Beister, J. Reschke and G. Hoelzsch, (1987), *J. Vac. Sci. Technol.*, A52188
  47. W.-D. Münz, (1986) *J. Vac. Sci. Technol.*, VA4, 2717
  48. W.D. Sproul, P.J. Rudnik, M.E. Graham and S.L. Rohde, (1990) *Surface and Coatings Technology*, V43/44270-278.
  49. W.D. Sproul, P.J. Rudnik, M.E. Graham and S.L. Rohde, (1990), *Surface and Coating Technology*, V43/44 117.
  50. W.D. Sproul, P.J. Rudnik, M.E. Graham and S.L. Rohde, (1990), *Surface and Coating Technology*, V43/44 270.
  51. S. Kadlec, J. Musil, V. Valaoda, W.-D. Münz, H. Petersein and J. Schroeder, (1990), *Vacuum*, V412233
  52. J.A. Venables, G.D.T. Spiller, M. Hanbucker, (1984), *Rep.Prog.Phys.*, 47, 399.
  53. M.Prutton, "Surface Physics", Oxford University Press, United Kingdom, 1983.
  54. L.D. Schepper, M.D'Olieslaeger, G.Knuyt, L.M. Stals, M.V. Stappen, B.Malliet, J.P.Celis and J.R.Roos, (1989), *Thin Solid Films*, 173, 199.
  55. J.Hong, G.S. Was, J.W. Jones, N.R. Moody, (May 1997), *J.Appl.Phys.*, Vol.81, No. 10, 15 .
  56. R.Carel, C.V. Thompson and H.J. Frost, (1996), *Acta mater*, Vol.44. No. 6, pp. 2479-2494.
  57. C.V. Thompson, R.Carel, (1995), *Materials Science and Engineering B32*

- 211-219.
58. C.V. Thompson, (1993), *Scripta Metallurgica et Materialia*, Vol.28, pp. 167-172.
59. C.V. Thompson and R. Carel, (1996), *Materials Science Forum Vols*, 204-206, pp.83-98.
60. C.V. Thompson and R.Carel, (1996), *J.Mech.Phys.Solids*.Vol.44.No5, pp.657-673.
61. C.V. Thompson and R.Carel, (1996), *Materials Science Forum Vols*. 204-206, pp.83-98.
62. P. Ding, Z. Ni, S. Zhou and F. Pan, (1991), *Surface and Coating Technology*, V49, 203.
63. E. Bauer and H. Poppa, (1972), *Thin Solid Films*, V12 167.
64. B.A. Movchan and A.V. Demshishin, (1969), *Fiz. Metal. Metalloved.* V28, 653.
65. J.A. Thornton, (1974) *Journal of Vacuum Science Technology*, V11, 666.
66. R. Messier, A.P. Giri and A. Roy, (1984), *Journal of Vacuum Science Technology*, A2, 500.
67. D.J. Srolovitz, A. Mazor, and G. Bukiet, (1988).*J.Vac.Sci.Technol.*, A6, 2371.
68. R.F. Carel, C.V. Thompson and H.J. Frost, (1996), *Acta mater.* Vol 44, No. 6, pp. 2479-2494.
69. C. V. Thompson and R. Carel, (1995), *Materials Science and Engineering* **B32**211-219.
- 70.. E.M. Zielinski, R.P. Vinci and J.C. Bravman, (1994) *J.Appl.Phys.* **76** (8), .
- 71 J.E. Sanchez Jr., E. Arzt, (1992), *Scripta Metallurgica et Materialia*, Vol 27, pp. 285-290
72. C.V. Thompson, (1993), *Scripta Metallurgica et Materialia*, Vol. 28, pp. 167-172.
73. G.B Harris, (1952), *Phil.Mag.*, **43** 113-123.
74. D.S. Rickerby, G.Eckold, K.T. Scott, I.M. Buckley-Golder, (1987), *Thin Solid Films*, **154**, 125.
75. O.Knotek, R.Elsing, G.Krämer, K.Jungblut, (1991), *Surf.Coat.Technol.*, **46**, 265-274.

- 76.. G. Abruzzese and P. Brozzo (Eds.), (1992), *Materials Science Forum*, Volumes 94-96, Pts.1&2.
77. C.V. Thompson, (1993), *Scripta Metallurgica et Materialia*, Vol. 28, pp.167-172.
78. C.V. Thompson and R. Carel, (1995), *Materials Science and Engineering*, B32, pp211-219.
79. R.E. Reed-Hill and R. Abbaschian, *Physical Metallurgy Principles*, third edition, PWS-Kent publishing company, 1992.
80. L. Vegard (1928) *Z.Krist.* **67**, 239.
81. H.J. Goldschmidt and J.A. Brand (1961) *J.Less-Common Metals*, 3, 44.
82. V.P. Eljutin and V.F. Funke (1956) *Izv. Akad. Nauk SSSR Otdel. Tekh. Nauk*, No. 3, 68
83. Nb-Cr phase diagrams, Binary Alloy Phase Diagrams, 2nd edition, ASM International, 1990.
84. H.Stuart, *Niobium*, TMS-AIME, Pittsburgh, PA, 1984, p.533.
85. K.J.A. Mawella and J.A. Sheward, (1990), *Thin Solid Films*, 19327.
86. Metals Handbook, Vol.2, ASM, Metals Park, OH, 1990, p.1144, 10th edn.
87. F.A. Smidt, (1990), *Int. Mater. Rev.*, 35 61.
88. D.M. Mattox, *J. Vac. Sci. Technol. A*, 7 (1989) 1105.
89. J.H. Hsieh, W. Wu, R.A. Erck, G.R. Fenske, Y.Y. Su, and M. Marek, (1992) *Surf.Coat.Technol.*, 51 212-216.
90. D.M. Turley, (1989), *Surf. Coat. Technol.*, 39-40 135.
91. I.M. Hutchings, *Tribology*, CRC Press, Boca Raton, FL, 1992, p.92.
92. B.D. Cullity, "Elements of X-Ray Diffraction", (second edition), Addison-Wesley publishing company, Inc. 1978.
92. G.B Harris, (1952), *Phil.Mag.*, 43 113-123.
93. B.D. Cullity, *Elements of X-Ray Diffraction*, Second Ed., p277, Addison-Wesley Publishing Company, Inc.
94. J.A. Sue and G.S.Schajer, "Stress Determination for Coatings", ASM Handbook, Vol.5, pp 647-653.
95. A.J. Perry, *et al*, (1996), *Surf, Coat, Tech.* **81**, 17-28.
96. B.D. Cullity, *Elements of X-Ray Diffraction*, Second Ed., p281, Addison-Wesley Publishing

- Company, Inc.
97. A.R. Gabriel - "*SEM-A users Manual for Materials Science*", 1972, North-Holland Press.
  98. D.A. Jones, *Principles and Prevention of Corrosion*, Macmillan Publishing Company 1992, 2nd edn.
  99. Verein Deutscher Ingenieure, *Richtlinie 3198*, 1992, Dusseldorf, F.R.G.
  100. B.D. Cullity, "Elements of X-Ray Diffraction", (second edition), Addison-Wesley publishing company, Inc. 1978.
  101. Y. Ding, Z. Farhat, D.O. Northwood, A.T. Alpas, *Surf. Coat. Technol.*, 68/69 (1994) 459-467.
  102. J.H.Hsieh, W.Wu, R.A.Erck, G.R.Fenske, Y.Y.Su and M.Marek, *Surface and Coatings Technology*, 51 (1992) 212-216.
  103. C.J. Brooker, RARDE Memorandum 92/84, 1984.
  104. K.J.A. Mawella and J.A. Sheward, International Conference on Ion and Plasma Assisted Techniques, (IPAT), Geneva, pp70-75, 1989.
  105. C.V. Thompson and R.Carel, *Materials Science and Engineering*, B32 (1995), pp211-219.

## 8. Appendix 1: Calculation of the theoretical X-ray peak intensities

The theoretical peak intensity is given by equation 8.1

$$|R_{hkl}| = Q.S. \frac{1}{\sin\theta} \left[ \frac{\sin\theta}{2\mu} \right] \left[ 1 - e^{-\frac{\sin\theta}{2\mu} x} \right]$$

where S is the area of the beam

x is the coating thickness

$\mu$  is the absorption coefficient for the material

$$\text{and } Q = \frac{1}{V^2} [F^2 P(LP)] \cdot [e^{-2m}]$$

where F is the structure factor

P is the multiplicity factor

m is the temperature factor

V is the volume of the unit cell

and LP is the Lorentz polarisation factor given by

$$LP = \frac{1 + \cos^2 2\theta}{\sin^2 \theta \cos\theta}$$

where  $2\theta$  is the angle between the beam and the surface